

## Article

# Improved Route to Linear Triblock Copolymers by Coupling with Glycidyl Ether-Activated Poly(ethylene oxide) Chains

Daniel T. Krause <sup>1,\*</sup> , Susanna Krämer <sup>1</sup>, Vassilios Siozios <sup>2</sup>, Andreas J. Butzelaar <sup>3</sup>, Martin Dulle <sup>4</sup>, Beate Förster <sup>5</sup> , Patrick Theato <sup>3,6</sup> , Joachim Mayer <sup>7,8</sup> , Martin Winter <sup>1,2</sup>, Stephan Förster <sup>4,9</sup>, Hans-Dieter Wiemhöfer <sup>1,\*</sup> and Mariano Grünebaum <sup>1,\*</sup> 

- <sup>1</sup> Helmholtz Institute Münster, IEK-12, Forschungszentrum Jülich GmbH, Corrensstr. 46, 48149 Münster, Germany
- <sup>2</sup> MEET Battery Research Center, University of Münster, Corrensstr. 46, 48149 Münster, Germany
- <sup>3</sup> Karlsruhe Institute of Technology (KIT), Institute for Chemical Technology and Polymer Chemistry (ITCP), Engesserstraße 18, 76131 Karlsruhe, Germany
- <sup>4</sup> Jülich Centre for Neutron Science (JCNS-1/IBI-8), Forschungszentrum Jülich, Wilhelm-Johnen-Straße, 52425 Jülich, Germany
- <sup>5</sup> Ernst Ruska-Centre for Microscopy and Spectroscopy with Electrons, Physics of Nanoscale Systems (ER-C-1), Forschungszentrum Jülich, Wilhelm-Johnen-Straße, 52425 Jülich, Germany
- <sup>6</sup> Soft Matter Synthesis Laboratory, Institute for Biological Interfaces 3 (IBG-3), Karlsruhe Institute of Technology (KIT), Hermann-von-Helmholtz-Platz 1, 76344 Eggenstein-Leopoldshafen, Germany
- <sup>7</sup> Ernst Ruska-Centre for Microscopy and Spectroscopy with Electrons, Materials Science and Technology (ER-C-2), Forschungszentrum Jülich GmbH, Wilhelm-Johnen-Straße, Jülich 52425, Germany
- <sup>8</sup> Jülich-Aachen Research Alliance, JARA, Fundamentals of Future Information Technology, Wilhelm-Johnen-Straße, 52425 Jülich, Germany
- <sup>9</sup> Institute of Physical Chemistry, RWTH Aachen University, Landoltweg 2, 52074 Aachen, Germany
- \* Correspondence: d\_krau05@uni-muenster.de (D.T.K.); h.wiemhoefer@fz-juelich.de (H.-D.W.); m.gruenebaum@fz-juelich.de (M.G.)



**Citation:** Krause, D.T.; Krämer, S.; Siozios, V.; Butzelaar, A.J.; Dulle, M.; Förster, B.; Theato, P.; Mayer, J.; Winter, M.; Förster, S.; et al. Improved Route to Linear Triblock Copolymers by Coupling with Glycidyl Ether-Activated Poly(ethylene oxide) Chains. *Polymers* **2023**, *15*, 2128. <https://doi.org/10.3390/polym15092128>

Academic Editor: Hui Sun

Received: 21 March 2023

Revised: 19 April 2023

Accepted: 27 April 2023

Published: 29 April 2023



**Copyright:** © 2023 by the authors. Licensee MDPI, Basel, Switzerland. This article is an open access article distributed under the terms and conditions of the Creative Commons Attribution (CC BY) license (<https://creativecommons.org/licenses/by/4.0/>).

**Abstract:** Poly(ethylene oxide) block copolymers (PEO<sub>z</sub> BCP) have been demonstrated to exhibit remarkably high lithium ion (Li<sup>+</sup>) conductivity for Li<sup>+</sup> batteries applications. For linear poly(isoprene)-*b*-poly(styrene)-*b*-poly(ethylene oxide) triblock copolymers (PI<sub>x</sub>PS<sub>y</sub>PEO<sub>z</sub>), a pronounced maximum ion conductivity was reported for short PEO<sub>z</sub> molecular weights around 2 kg mol<sup>-1</sup>. To later enable a systematic exploration of the influence of the PI<sub>x</sub> and PS<sub>y</sub> block lengths and related morphologies on the ion conductivity, a synthetic method is needed where the short PEO<sub>z</sub> block length can be kept constant, while the PI<sub>x</sub> and PS<sub>y</sub> block lengths could be systematically and independently varied. Here, we introduce a glycidyl ether route that allows covalent attachment of pre-synthesized glycidyl-end functionalized PEO<sub>z</sub> chains to terminate PI<sub>x</sub>PS<sub>y</sub> BCPs. The attachment proceeds to full conversion in a simplified and reproducible one-pot polymerization such that PI<sub>x</sub>PS<sub>y</sub>PEO<sub>z</sub> with narrow chain length distribution and a fixed PEO<sub>z</sub> block length of  $z = 1.9$  kg mol<sup>-1</sup> and a  $D = 1.03$  are obtained. The successful quantitative end group modification of the PEO<sub>z</sub> block was verified by nuclear magnetic resonance (NMR) spectroscopy, gel permeation chromatography (GPC) and differential scanning calorimetry (DSC). We demonstrate further that with a controlled casting process, ordered microphases with macroscopic long-range directional order can be fabricated, as demonstrated by small-angle X-ray scattering (SAXS), scanning electron microscopy (SEM) and transmission electron microscopy (TEM). It has already been shown in a patent, published by us, that BCPs from the synthesis method presented here exhibit comparable or even higher ionic conductivities than those previously published. Therefore, this PEO<sub>z</sub> BCP system is ideally suitable to relate BCP morphology, order and orientation to macroscopic Li<sup>+</sup> conductivity in Li<sup>+</sup> batteries.

**Keywords:** polymers; block copolymers; polyethylene oxide (PEO); convergent synthesis; epoxide; anionic polymerization; microphase separation; morphology

## 1. Introduction

As a polymer class, block copolymers (BCPs) are gaining continuous attention due to their remarkable properties such as an amphiphilic character or self-assembling ability [1–3]. For instance, an amphiphilic behavior enables in solution the formation of micelles, which are widely utilized in pharmaceutical applications, e.g., for drug delivery systems [1,2]. Moreover, their ability to self-assemble also in bulk paves the way to well-ordered morphologies, which find a wide range of applications [3–5], e.g., in lithography [6], semiconductor-based photocatalysis [4,7] and energy storage and conversion as fuel cell membranes [8], electrodes [9] or polymer electrolytes [10–12].

These aforementioned properties rely on the tailorable and unique structure of the respective BCP. The covalent binding of polar and nonpolar polymer blocks with defined block length could result in macromolecules with amphiphilic character and therefore tend to organize themselves into periodic, highly ordered, nano-sized domains, the so-called microphases [3–6,8,13–16]. The Flory–Huggins interaction parameter ( $\chi$ ) quantifies the incompatibility between the different blocks based on their interaction energy [13–16].

Our decision to choose the linear triblock copolymer poly(isoprene)-*b*-poly(styrene)-*b*-poly(ethylene oxide), denoted as PI<sub>x</sub>PS<sub>y</sub>PEO<sub>z</sub>, whereby each index (*x*, *y* and *z*) indicates the molar mass ( $M_n$ ) of the corresponding block in kg mol<sup>−1</sup>, was inspired by the work of Dörr et al. [4,7–11]. They applied a synthetic route developed in the group of Bates [17–19] and demonstrated its advantageous use as a template for detailed control of mesoscopic porous 3D architectures with embedded inorganic materials [4,7–11]. In our case, the synthesized PI<sub>x</sub>PS<sub>y</sub>PEO<sub>z</sub> are supposed to be used as a structure-giving BCP matrix for conducting lithium ions (Li<sup>+</sup>). Additionally, Dörr and Pelz et al. showed that lowering the PEO<sub>z</sub> chain length down to values around 45 repeating units ( $M_n \sim 2$  kg mol<sup>−1</sup>) and with a low content (<4 vol.%) in relation to total BCP size resulted in a high Li<sup>+</sup> conductivity [10,11].

Therefore, the PEO<sub>z</sub> block has a significant influence on the Li<sup>+</sup> transport properties and is directly linked to it, as the Li<sup>+</sup> presumably only accumulate in this block, resulting in the formation of Li<sup>+</sup> conducting pathways [10,11,20]. Consequently, those Li<sup>+</sup> conducting pathways and, finally, the total Li<sup>+</sup> transport are substantially determined by the properties of the PEO<sub>z</sub> block and its resulting domain structure such as its size, long-range order, morphology and macroscopic orientation. This means for an optimal Li<sup>+</sup> transfer, the structure-giving BCP matrix has to arrange itself into a long-range and highly ordered morphology, e.g., lamellar (LAM) or hexagonally close-packed cylindrical (HEX), continuously between two electrodes and an orientation connecting these electrodes. In order to obtain these properties in the PI<sub>x</sub>PS<sub>y</sub>PEO<sub>z</sub>, the combination of always having precisely defined length and a nearly monodisperse distribution in each block, as well as a controlled self-assembly during the membrane preparation process, is important [21,22].

Hence, in this work, the influence of the structure-giving BCP matrix on the short PEO<sub>z</sub> chain order will be investigated. Corresponding PI<sub>x</sub>PS<sub>y</sub>PEO<sub>z</sub> BCP will be synthesized by keeping the PEO<sub>z</sub> chain length constant in order to vary its composition systematically and independently from each other (cf. Scheme 1) [18,19,23,24]. For this purpose, PI<sub>x</sub>PS<sub>y</sub>PEO<sub>z</sub> BCPs are varied in two different ways:

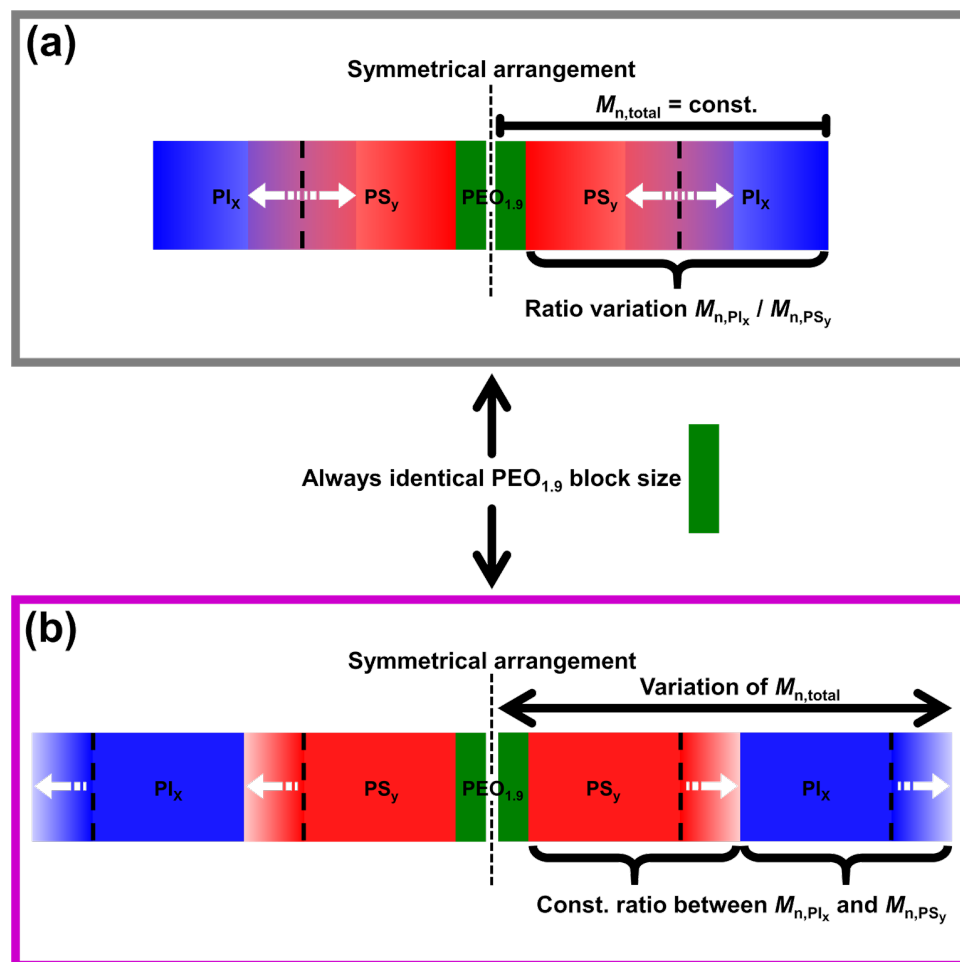
(1) By differing the ratio of the  $M_n$  of the PI<sub>x</sub> to the PS<sub>y</sub> block ( $M_{n,PIx}/M_{n,PSy}$ ), while retaining the same PEO<sub>z</sub> block proportion because the total  $M_n$  of the BCP ( $M_{n,total}$ ) is hold constant (cf. Scheme 1a).

(2) By altering the  $M_{n,total}$  and therefore the PEO<sub>z</sub> block proportion, while keeping  $M_{n,PIx}/M_{n,PSy} = \text{constant}$  (cf. Scheme 1b).

This will be achieved by a new developed synthesis route, which ensures the use of consistent identical and very short as well as commercially available prefabricated PEO<sub>z</sub> chains for the attachment to BCPs.

Usually, such BCPs are prepared in a stepwise manner by synthesizing each polymer block sequentially [17–19,25]. Thus, each polymer block is formed from the respective monomers in a series of polymerization steps according to the principle of living sequential anionic polymerization (cf. Scheme 2I), as it offers the highest control over the polymerization

process, hence the dispersity ( $\mathcal{D}$ ), and also proceeds without side reactions [5,17–19,26–29]. However, due to the explosive and highly toxic properties of ethylene oxide (EO) gas, its use implies special safety requirements [30]. Therefore, the use of a short prefabricated PEO<sub>z</sub> block in our synthesis route leads to the fact that the handling of EO gas monomers during PI<sub>x</sub>PS<sub>y</sub>PEO<sub>z</sub> polymerization can be avoided. In this way, the necessary use of EO gas for the synthesis of PEO<sub>z</sub> chains can be carried out in a separate and upstream synthesis step.

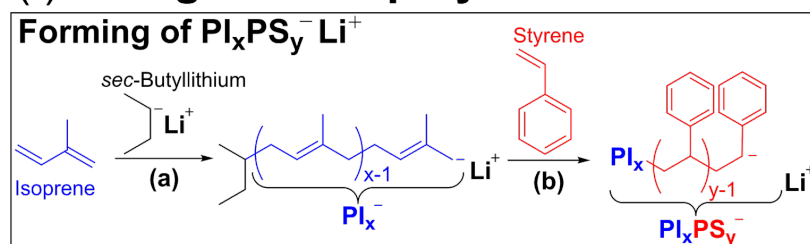


**Scheme 1.** Controlled compositional variations of the synthesized PI<sub>x</sub>PS<sub>y</sub>PEO<sub>z</sub> BCP by systematically and independently altering the PI<sub>x</sub> and PS<sub>y</sub> block lengths while keeping the PEO<sub>z</sub> block constant. (a) Changing the ratio of the  $M_n$  of the PI<sub>x</sub> to the PS<sub>y</sub> block ( $M_{n,PI_x} / M_{n,PS_y}$ ) by keeping the total  $M_n$  of the BCP ( $M_{n,total}$ ) constant and therefore retaining identical PEO<sub>z</sub> block proportion. (b) Variation of the PEO<sub>z</sub> block proportion in the BCP by altering the  $M_{n,total}$  and holding  $M_{n,PI_x} / M_{n,PS_y} = \text{constant}$ .

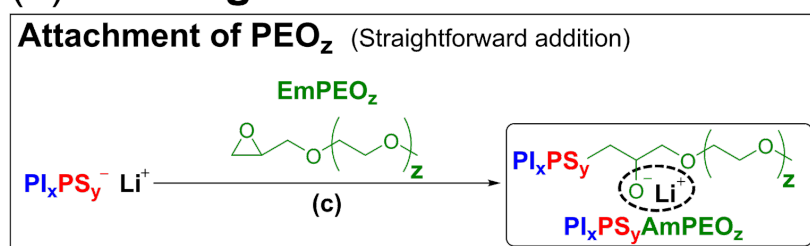
Thus, in this study, an exact defined methoxy PEO (mPEO<sub>z</sub>) chain with a modified end group was chosen, enabling it accessible for direct and covalent attachment to the stable PI<sub>x</sub>PS<sub>y</sub><sup>−</sup> carbanion of the living polymer chain. Considering the large variety of suitable end groups, tethering an epoxide end group to the mPEO<sub>z</sub> chain (EmPEO<sub>z</sub>) enables a selective single one-step addition to the PI<sub>x</sub>PS<sub>y</sub><sup>−</sup> anion by utilization of the strong Li-O interaction (cf. Scheme 2II) [5,17,31–34]. This is similar to the general strategy of using epoxides as terminating agents as reported in literature [35–41]. The strong interaction between the hard oxygen anion and the hard Li<sup>+</sup> can be well explained based on the concept of “hard” and “soft” acids and bases (HSAB) [32,42]. In addition to the PEO<sub>z</sub> chain, at the junction point only an extra alcohol group is introduced in the polymer as (poly(isoprene)-*b*-poly(styrene)-*b*-alcohol methoxy poly(ethylene oxide) = PI<sub>x</sub>PS<sub>y</sub>AmPEO<sub>z</sub>).

Our convergent synthetic method based on the modular principle aims to create access to  $PI_xPS_yPEO_z$  with constantly the same very short and well-defined  $PEO_z$  block, allowing the  $PI_x$  and  $PS_y$  blocks to be varied systematically and independently. Moreover, as this synthesis route only utilizes commercially available chemicals, it offers a high reproducibility and up-scaling probability, making tailored and precisely defined  $PI_xPS_yAmPEO_z$  BCPs accessible for large-scale production. We have already published a prior patent application for this synthesis method [43].

## (I) Living anionic polymerization



## (II) Convergent termination



**Scheme 2.** Synthesis routes towards  $PI_xPS_yPEO_z$  triblock copolymers. (I) Illustration of the living anionic polymerization forming the  $PI_xPS_y^- Li^+$  anion with  $Li^+$  as counterion, whereas each block is obtained from the respective monomers. (II) Final linkage of the  $PEO_z$  block to the  $PI_xPS_y^- Li^+$  anion using EmPEO<sub>z</sub>. The formation of the O-Li-ion pair inhibits further ring-opening polymerization and is highlighted by a dotted circle. For clarity, the *sec*-butyl group resulting from *sec*-butyllithium is drawn only once at the beginning.

## 2. Materials and Methods

### 2.1. Materials

Sodium *tert*-butoxide (NaO<sup>t</sup>Bu, 99.9%, Sigma-Aldrich, Darmstadt, Germany) was purified by sublimation [44] (105 °C at  $\leq 3 \times 10^{-3}$  mbar), 3 Å molecular sieves (VWR, Darmstadt, Germany) was activated by drying at 300 °C under vacuum  $< 1 \times 10^{-6}$  mbar and methoxy poly(ethylene oxide) (mPEO<sub>1.9</sub> equals to  $M_n = 1.9$  kg mol<sup>-1</sup>, VWR) was dried at 30 °C under vacuum  $< 1 \times 10^{-6}$  mbar and all were subsequently stored inside a glovebox (MBraun Unilab, Garching, Germany,  $\leq 0.1$  ppm of Water (H<sub>2</sub>O) and oxygen (O<sub>2</sub>)) under argon atmosphere. Epichlorohydrin ( $\geq 99.0\%$ , Sigma-Aldrich), chloroform-*d*<sub>1</sub> (CDCl<sub>3</sub>, 99.8% D, VWR) and toluene ( $\geq 99.85\%$ , VWR) were dried using activated 3 Å molecular sieves until  $\leq 1$  ppm H<sub>2</sub>O, tetrahydrofuran (THF,  $\geq 99.8\%$ , unstab., Alfa Aesar, Kandel, Germany) was dried using activated 3 Å molecular sieves until  $\leq 5$  ppm H<sub>2</sub>O; all were subsequently stored inside a glovebox under argon atmosphere and passed through syringe filter (polytetrafluoroethylene (PTFE) membrane, pore size = 0.2 μm, VWR) prior to use. Seven days before use, isoprene ( $\geq 99\%$ , VWR) and styrene ( $\geq 99\%$ , Sigma-Aldrich) were dried (still stored in glovebox fridge) using activated 3 Å molecular sieves until  $\leq 1$  ppm H<sub>2</sub>O and were distilled under vacuum directly before use. A total of 1.4 M *sec*-butyllithium solution in cyclohexane (*sec*-BuLi, Sigma-Aldrich) was used as received. The concentration of *sec*-BuLi was directly determined by double titration, using a glass-coated magnetic stir bar and the ready-to-use reagent: 2-propanol solution in toluene

with 0.2% 1,10 phenanthroline indicator titration solution for quantitative analysis of butyllithium (Sigma-Aldrich), prior to use. Diethyl ether (Et<sub>2</sub>O, ≥99.9%, inhibitor-free, Sigma-Aldrich), dichloromethane (DCM, ≥99.5%, VWR), methanol (MeOH, ≥99.9%, VWR) and 0.5 M hydrogen chloride solution in MeOH (Sigma-Aldrich) were used as received. For quantitative water content determination, a Karl Fischer coulometric titrator C30S (Mettler-Toledo, Gießen, Germany) with a platinum generator electrode without a diaphragm was used.

## 2.2. End Group Modification (EmPEO<sub>1,9</sub>)

The complete end group modification reaction of mPEO<sub>1,9</sub> to EmPEO<sub>1,9</sub> was carried out at room temperature under argon atmosphere in a glovebox. NaO<sup>t</sup>Bu (1.5 equiv, 9.32 mmol, 0.896 g) was dissolved in THF (60 mL) and subsequently added to a solution of mPEO<sub>1,9</sub> (1.0 equiv, 6.29 mmol, 12.0 g) in THF (60 mL). After 72 h, epichlorohydrin (8.0 equiv, 50.3 mmol, 4.65 g, 3.94 mL) was added dropwise to the reaction within 15 min and stirred for six days. Subsequently, the volatile components were removed at 55 °C under vacuum and the solid residue was dissolved in THF. Undissolved components, mainly formed sodium chloride (NaCl), were removed by centrifugation (Sigma 3-18KS, Osterode am Harz, Germany, 10000 rpm for 10 min), followed by filtration with syringe filter (PTFE membrane, pore size = 0.2 μm, VWR) and drying at room temperature under vacuum. Afterwards, the product was dissolved in a little amount of toluene at 40 °C, precipitated into cold Et<sub>2</sub>O and collected by centrifugation as before. This process was repeated three times. The resulting EmPEO<sub>1,9</sub> was dried at 30 °C under vacuum < 1 × 10<sup>-6</sup> mbar (yield: 89–93%). The product was characterized by <sup>1</sup>H-nuclear magnetic resonance (NMR) spectroscopy, <sup>13</sup>C-NMR spectroscopy, gel permeation chromatography (GPC), differential scanning calorimetry (DSC) and thermogravimetric analysis (TGA).

## 2.3. Synthesis of Poly(isoprene)-*b*-poly(styrene)-*b*-alcohol Methoxy Poly(ethylene oxide) (PI<sub>x</sub>PS<sub>y</sub>AmPEO<sub>1,9</sub>)

The complete polymer synthesis reaction of PI<sub>x</sub>PS<sub>y</sub>AmPEO<sub>1,9</sub> was carried out at room temperature under argon atmosphere in a glovebox using a glass-coated magnetic stir bar for mixing. The PI<sub>x</sub> and PS<sub>y</sub> block was synthesized by living sequential anionic polymerization as reported in the literature (Scheme 2I) [17–19]. All PI<sub>x</sub>PS<sub>y</sub>AmPEO<sub>1,9</sub> materials were synthesized, as exemplarily described for the PI<sub>14.6</sub>PS<sub>34.8</sub>AmPEO<sub>1,9</sub> in the following, where only the *sec*-BuLi, monomers (isoprene and styrene) and EmPEO<sub>1,9</sub> amounts were adjusted according to the desired composition (cf. Table 1).

**Table 1.** Overview of *sec*-BuLi (initiator), monomers (isoprene and styrene) and EmPEO<sub>1,9</sub> used for the synthesis of PI<sub>x</sub>PS<sub>y</sub>AmPEO<sub>1,9</sub>.

Polymer	<i>n</i> ( <i>sec</i> -BuLi) /mmol	<i>n</i> (Isoprene) /mmol	<i>n</i> (Styrene) /mmol	<i>n</i> (EmPEO <sub>1,9</sub> ) /mmol
PI <sub>6.8</sub> PS <sub>17.3</sub> AmPEO <sub>1,9</sub>	0.256	25.6	42.5	0.282
PI <sub>14.6</sub> PS <sub>34.8</sub> AmPEO <sub>1,9</sub>	0.249	53.1	83.1	0.274
PI <sub>24.8</sub> PS <sub>25.0</sub> AmPEO <sub>1,9</sub>	0.132	48.0	31.5	0.145
PI <sub>35.1</sub> PS <sub>14.8</sub> AmPEO <sub>1,9</sub>	0.233	119.9	33.2	0.257
PI <sub>26.1</sub> PS <sub>67.3</sub> AmPEO <sub>1,9</sub>	0.148	56.6	95.3	0.163

For preparation of the PI<sub>14.6</sub> block, isoprene (214 equiv, 53.1 mmol, 3.62 g) was dissolved in toluene (120 mL) followed by the addition of 1.4 M *sec*-BuLi solution in cyclohexane (1.0 equiv, 0.249 mmol, 178 μL). After stirring for 24 h, to ensure a quantitative conversion of isoprene monomers [45], styrene (334 equiv, 83.1 mmol, 8.66 g) was added to the yellowish reaction solution of the living PI<sub>14.6</sub><sup>-</sup> anion to build the PS<sub>34.8</sub> block. After stirring for 24 h, to ensure a quantitative conversion of styrene monomers [45], EmPEO<sub>1,9</sub> (1.1 equiv, 0.274 mmol, 0.521 g) was added to the reddish reaction solution

of the living  $PI_{14.6}PS_{34.8}^-$  anion to attach the  $PEO_{1.9}$  block. After stirring for 48 h, 0.5 M hydrogen chloride solution in MeOH (1.5 equiv, 0.37 mmol, 497  $\mu$ L) was added to the colorless reaction solution. Subsequently, the volatile components were removed at 40 °C under vacuum. Then, the product was dissolved in DCM, precipitated into MeOH and this process was repeated three times. The resulting polymer was dried at 50 °C under vacuum  $< 1 \times 10^{-6}$  mbar (yield: 92–95%). The product was obtained as a white solid and characterized by  $^1H$ -NMR spectroscopy, GPC, DSC and TGA.

#### 2.4. Sample Preparation of $PI_xPS_yAmPEO_{1.9}$ Membranes for Morphological Characterization

The complete  $PI_xPS_yAmPEO_{1.9}$  membrane casting process, for preparing the samples for the morphological characterization, was performed under argon atmosphere. In a glovebox, an 8 wt.% solution of the dried  $PI_xPS_yAmPEO_{1.9}$  in THF was prepared and followed by transferring the mixture into a PTFE crucible. The filled PTFE crucible was placed in a Schlenk vessel and connected to the argon of a Schlenk line. A very low and constant argon flow over 6 days at room temperature in a THF-saturated atmosphere was used to allow a controlled evaporation to achieve distinct microphase separation.

Subsequently, for small-angle X-ray scattering (SAXS) measurement, the resulting membrane (cf. Figure S17) was carefully broken into smaller pieces in order to fit the sample into the glass capillary (borosilicate glass, outer diameter = 2.1 mm, wall thickness = 0.05 mm, Hilgenberg, Malsfeld, Germany). The filled glass capillary was sealed tightly.

For scanning electron microscopy (SEM) and transmission electron microscopy (TEM) investigations, a small piece of the resulting membrane (cf. Figure S17) was cut into ultrathin sections of about 50–100 nm using a cryo-ultramicrotome (cf. Scheme S2).

#### 2.5. Nuclear Magnetic Resonance (NMR) Spectroscopy

The NMR spectra of  $PI_{14.6}PS_{34.8}AmPEO_{1.9}$ ,  $PI_{35.1}PS_{14.8}AmPEO_{1.9}$  and  $EmPEO_{1.9}$  were recorded using an AVANCE NEO 500 MHz (Bruker, Billerica, MA, USA), that of  $mPEO_{1.9}$ ,  $PI_{24.8}PS_{25.0}AmPEO_{1.9}$  and  $PI_{26.1}PS_{67.3}AmPEO_{1.9}$  using an AVANCE NEO 400 MHz (Bruker) and for  $PI_{6.8}PS_{17.3}AmPEO_{1.9}$  using an AVANCE III 400 MHz (Bruker). NMR measurements with number of scans = 64 were recorded, and the recycle delay  $D1$  between transients was set to 30 s to ensure full relaxation to equilibrium magnetization and thus the acquisition of quantitative spectra, except for  $mPEO_{1.9}$ . All NMR spectra were recorded at 300 K using  $CDCl_3$  as deuterated solvent, where all signals were referenced to  $CDCl_3$  ( $\delta = 7.3$  ppm for  $^1H$  and  $\delta = 77.2$  ppm for  $^{13}C$  relative to tetramethylsilane) [46]. The spectra were analyzed with the software MestReNova (version: 12.0.4-22023, Mestrelab Research, Santiago de Compostela, Spain).

#### 2.6. Gel Permeation Chromatography (GPC)

GPC was carried out in THF using an HLC-8320GPC EcoSEC (Tosoh Bioscience, Griesheim, Germany) system equipped with three PSS SDV columns (100, 1000, 100,000 Å) ( $8 \times 300$  mm) of 5  $\mu$ m, a UV and a differential refractive index (RI) detector. The operation temperature was set to 35 °C with a flow rate of 1 mL  $min^{-1}$ . Calibration of the system was carried out with poly(styrene) standards ranging from 800 to  $2.2 \times 10^6$  g  $mol^{-1}$ . Typically, 50  $\mu$ L of a 2.0 mg  $mL^{-1}$  sample solution was injected onto the columns.

#### 2.7. Differential Scanning Calorimetry (DSC)

DSC was conducted using a heat flux calorimeter DSC-Q2000 (TA Instruments, New Castle, DE, USA) with LNCS (Liquid Nitrogen Cooling System) and the Tzero<sup>®</sup>-technology for the precise recording of the baseline. Under argon atmosphere (inside glovebox), ~10 mg of sample was enclosed in hermetically sealed Tzero<sup>®</sup> aluminum pans. Two heating ramps in the temperature range from  $-140$  °C to 190 °C with a heating rate of 10 K  $min^{-1}$  under helium as sample purge (25 mL  $min^{-1}$ ) were measured for all samples. The DSC signals were analyzed with the Universal Analysis 2000 software (version: 4.5A, Build 4.5.0.5, TA Instruments).

### 2.8. Thermogravimetric Analysis (TGA)

For TGA, an aluminum pan was filled with ~10 mg of sample and hermetically sealed under argon atmosphere in a glovebox, subsequently loaded to the device without contact to ambient air and pierced in the furnace under helium atmosphere. The measurement was carried out on a TGA-5500 with IR furnace (TA Instruments) under helium flow ( $25 \text{ mL min}^{-1}$ ) with a constant heating rate of  $2 \text{ K min}^{-1}$  from  $30 \text{ }^\circ\text{C}$  to  $600 \text{ }^\circ\text{C}$ . The TGA signals were analyzed with the TA Instruments TRIOS software (version: 5.1.1.46572, TA Instruments).

### 2.9. Small-Angle X-ray Scattering (SAXS)

The instruments “Ganesh-Air” from SAXSLAB/XENOCs (Grenoble, France) and Gallium Anode Low-Angle X-ray Instrument (GALAXI) were used. The X-ray source of the laboratory-based “Ganesh-Air” system is a D2-MetalJet (Excillum, Kista, Sweden) with a liquid metal anode operating at 70 kV and 3.57 mA with Ga- $K\alpha$  radiation (wavelength  $\lambda = 0.134 \text{ nm}$ ). The beam is further focused with a focal length of 55 cm, using especially made X-ray optics (Xenocs) to provide a very narrow and intense beam at the sample position. Two pairs of scatterless slits are used to adjust the beam size depending on the detector distance. The data were acquired with a position-sensitive detector (PILATUS 300 K, Dectris, Baden-Daettwil, Switzerland). After calibration with silver behenate, the distance from the sample to the detector was set to 950 and 350 mm resulting in a  $Q$ -range  $0.13\text{--}6.00 \text{ nm}^{-1}$ . All samples were sealed in glass capillaries of 2 mm inner diameter. Data reduction and background subtraction were performed using the Python-based project Jscatter [47]. Fitting of radially averaged SAXS curves was done using Scatter [48].

### 2.10. Cryo-Ultramicrotomy

To prepare ultra-thin sections for electron microscopy, a Leica EM UC7 ultramicrotome (Wetzlar, Germany) equipped with an EM FC7 cryo-chamber was used. Temperature of sample, knives and chamber was set to  $-80 \text{ }^\circ\text{C}$ . The samples were trimmed with a diamond trimming knife from Diatome (trim 45, Nidau, Switzerland), and ultra-thin sections were made with a cryo-immuno diamond knife also from Diatome (cf. Scheme S2). Ultra-thin sections were collected dry on carbon-coated copper grids and section thickness was set to 50 nm.

### 2.11. Scanning Electron Microscope (SEM)

SEM measurements were performed using a Thermo-Fisher Volumescop (Waltham, MA, USA). Images were taken on unstained samples in high vacuum at an accelerating voltage of 30 kV and a working distance of 10 mm using an annular ring STEM detector in bright field mode at room temperature.

### 2.12. Transmission Electron Microscope (TEM)

For TEM measurements, a JEOL JEM-F200 (Freising, Germany) with field emission gun (FEG) operating at an accelerating voltage of 200 kV was used. Images were taken of the unstained sample with a STEM bright field detector at room temperature.

## 3. Results and Discussion

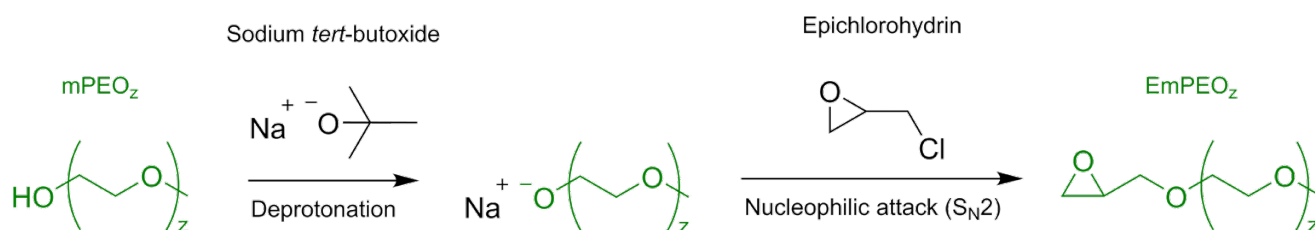
### 3.1. Strategy

In line with the introductory part, the main focus of this work is to develop a convergent synthesis route which enables the independent and systematic  $\text{PI}_x$  and  $\text{PS}_y$  block variation in BCPs with constantly the same  $\text{PEO}_z$  block size, whereby the complete control over morphology and orientation of the BCP, especially of the very short  $\text{PEO}_z$  block, should be obtained, as this is crucial for its possible application. For this purpose,  $\text{PEO}_z$  blocks with an identical chain length were chosen and introduced into  $\text{PI}_x\text{PS}_y\text{PEO}_z$ , in which the  $\text{PI}_x$  and  $\text{PS}_y$  blocks are synthesized by anionic polymerization of the monomers and therefore easily and precisely modified.

To do so, the commercially available and prefabricated  $\text{mPEO}_z$  ( $M_n = 1.9 \text{ kg mol}^{-1}$ ) was activated for the attachment by functionalization with an epoxide end group (yielding

EmPEO<sub>z</sub>). In our synthesis route, the EmPEO<sub>z</sub> can be attached and thus covalently linked to the previously anionically synthesized PI<sub>x</sub>PS<sub>y</sub><sup>−</sup> carbanion by a simple one-step addition (cf. Scheme 2). Herein, it is important that an appropriate end group is selected, because it will have a great influence on the properties of the whole PEO<sub>z</sub> block of the BCP, especially in our focus of very short PEO<sub>z</sub> chains [49]. Thus, the use of an epoxide as an end group ensures that the formed junction point in PI<sub>x</sub>PS<sub>y</sub>AmPEO<sub>z</sub> hardly differs from the PI<sub>x</sub>PS<sub>y</sub>PEO<sub>z</sub> obtained by using EO gas, i.e., only by an additional OH-group. This smallest possible difference enables the selective consideration solely of the variation of the two nonpolar blocks between the different synthesized PI<sub>x</sub>PS<sub>y</sub>AmPEO<sub>z</sub>. There are approaches that have been reported in literature thus far in which, for instance, benzophenone or diphenylethylene were attached to the PEO<sub>z</sub> chain as terminal groups [49]. However, regarding the reported end group modifications, multi-step synthesis has to be employed, making the overall synthesis of a PI<sub>x</sub>PS<sub>y</sub>PEO<sub>z</sub> more complex, and these groups are more chemically different compared to the ether and OH-group with unintended influence on the polarity [50]. Especially in the case of short PEO<sub>z</sub> chains, this could have a great impact on its domain structure formation.

Considering the end group modification shown in Scheme 3, the PEO<sub>z</sub> block was end-capped with an epoxide group in a simple literature-known and modified one-pot reaction [51,52]. In the first modification step, the terminal OH-group of mPEO<sub>z</sub> is selectively deprotonated by a strong base, i.e., NaO<sup>t</sup>Bu. Afterwards, the formed mPEO<sub>z</sub> alcoholate attacks the epoxide group of the added epichlorohydrin via a nucleophilic (S<sub>N</sub>2) attack to form the desired product EmPEO<sub>z</sub> (Scheme 3). This method can also be extended for longer ( $M_n = 6 \text{ kg mol}^{-1}$ ) PEO<sub>z</sub> chains as reported by van Butsele et al. [52]. Here it should be mentioned, that the PEO<sub>z</sub> block has to be selectively functionalized at only one terminal OH-group. End-capping both terminal OH-groups would lead to the undesired formation of a symmetric five BCP (PI<sub>x</sub>PS<sub>y</sub>PEO<sub>z</sub>PS<sub>y</sub>PI<sub>x</sub>). As mPEO<sub>z</sub> only possess one terminal OH-group allowing for a distinct functionalization, the linkage to the PI<sub>x</sub>PS<sub>y</sub><sup>−</sup> anion happens in a selective manner, as indicated in (Scheme 3).



**Scheme 3.** End group modification of mPEO<sub>z</sub> to selectively attach a terminal epoxide group to yield EmPEO<sub>z</sub>.

Another important aspect of the above-described usage of the prefabricated mPEO<sub>z</sub> block is the accurate characterization prior to its linkage, because a PEO<sub>z</sub> block that is already attached to the PI<sub>x</sub>PS<sub>y</sub> block is relatively small compared to the total BCP and therefore difficult to characterize and control accurately, especially in terms of its  $\bar{D}$ .

The straightforward addition of EmPEO<sub>z</sub> to the reaction solution furthermore simplifies the polymerization by terminating the living PI<sub>x</sub>PS<sub>y</sub><sup>−</sup> anion because it allows a one-step attachment in the presence of the Li<sup>+</sup> counterion in nonpolar solvent (Scheme 2II). After the addition of the EmPEO<sub>z</sub> to the reaction solution, the PI<sub>x</sub>PS<sub>y</sub><sup>−</sup> anion attacks the epoxy group of the EmPEO<sub>z</sub> via a ring-opening reaction forming an alcoholate group and a covalent bond between the PI<sub>x</sub>PS<sub>y</sub> block and the AmPEO<sub>z</sub>. Hence, the charge of the carbanion is transferred to the O-atom of the alcoholate group. The negative charge on the O-atom of the alcoholate group is directly blocked by the Li<sup>+</sup> counterion, which strongly reduces the nucleophilicity. Therefore, a new ring-opening reaction with another epoxide group of a second EmPEO<sub>z</sub> molecule is inhibited due to the strong O-Li-ion pair (Scheme S1), thus blocking a further polymerization, or any other undesired crosslinking or side reaction

and highlighting the advantage of this one-pot synthesis route (Scheme 2) [17,31,37–40]. Especially, a reaction of the living anions with  $O_2$  is suppressed, so that immediately after the AmPEO<sub>z</sub> block attachment, the product is stable in air, providing an advantage in terms of reproducibility and up-scalability [53–55].

Moreover, the epoxide functionalization allows the EmPEO<sub>z</sub> to be added to the reaction solution in minimal excess (cf. Table 1), so that the PI<sub>x</sub>PS<sub>y</sub><sup>−</sup> anions react stoichiometrically to form the PI<sub>x</sub>PS<sub>y</sub>AmPEO<sub>z</sub> and the excess and unbound EmPEO<sub>1.9</sub> is easily washed out after the polymerization reaction.

### 3.2. Synthesis

Triblock copolymers were synthesized in one-pot polymerization in three sequential steps by living anionic polymerization. As indicated by Scheme 2Ia, the PI<sub>x</sub> block was prepared from isoprene monomers using *sec*-BuLi serving as initiator for formation of the living carbanion. Subsequently, the living PI<sub>x</sub><sup>−</sup> anion was used for chain extension by addition of styrene (Scheme 2Ib). In the third step of this synthesis route, the PEO<sub>z</sub> block was covalently attached to the living PI<sub>x</sub>PS<sub>y</sub><sup>−</sup> anion via a one-step reaction of the epoxide group-functionalized EmPEO<sub>z</sub> and thus terminated the polymerization to the BCP (Scheme 2II). The coupling of EmPEO<sub>z</sub> to a PI<sub>x</sub>PS<sub>y</sub><sup>−</sup> anion enabled the selective and highly controllable preparation of PI<sub>x</sub>PS<sub>y</sub>AmPEO<sub>z</sub> in which the PEO<sub>1.9</sub> block features an identical chain length and a  $\bar{D}$  very close one in all cases. The respective  $M_{n,PI_x}/M_{n,PS_y}$  and thus the  $M_{n,total}$  of the BCP can be specifically tailored by systematically varying the used amount of initiator and the PI<sub>x</sub> and PS<sub>y</sub> monomers. However, as the living anionic polymerization is highly sensitive to impurities, because they directly lead to the termination of the corresponding living anion, special requirements for the synthesis conditions must always be ensured (cf. experimental section).

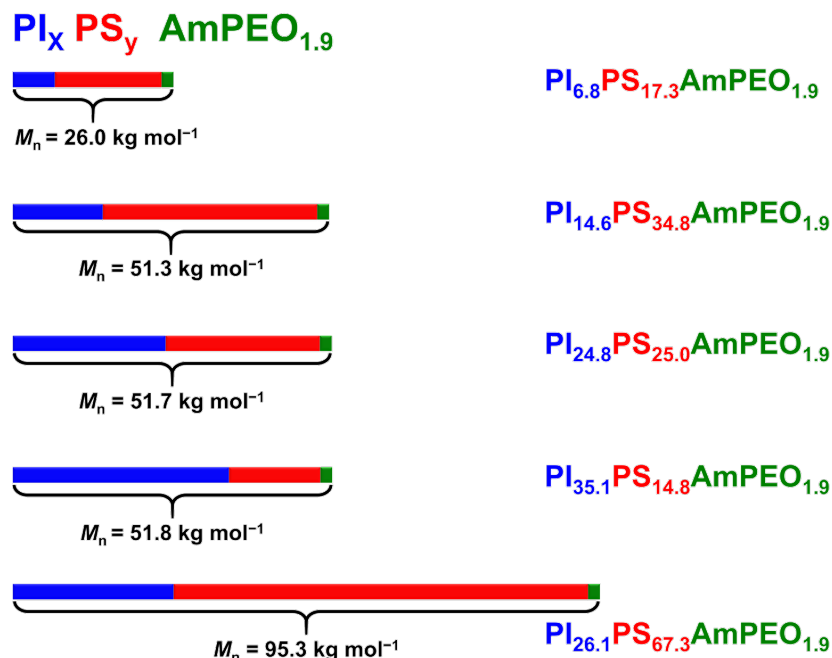
Here, it is worth noticing that the reaction of mPEO<sub>z</sub> to EmPEO<sub>z</sub> has to be quantitative, as no separation of both can be conducted due to the strong chemical similarity of mPEO<sub>z</sub> and EmPEO<sub>z</sub>. Even more, since acidic protons of residual mPEO<sub>z</sub> would protonate the PI<sub>x</sub>PS<sub>y</sub><sup>−</sup> anions upon addition and therefore inhibit the reaction of EmPEO<sub>z</sub> and the PI<sub>x</sub>PS<sub>y</sub><sup>−</sup> anions, the importance of a quantitative functionalization reaction is emphasized. In order to obtain a quantitative end group modification of mPEO<sub>z</sub>, the base used for deprotonation of the OH-group has to be a weak nucleophile, as otherwise it would compete with the formed mPEO<sub>z</sub> alcoholate regarding the S<sub>N</sub>2 reaction with epichlorohydrin, thus minimizing the yield of the desired EmPEO<sub>z</sub>. Additionally, the following conditions have been optimized for the quantitative formation of EmPEO<sub>z</sub>: (1) The use of NaO<sup>t</sup>Bu and epichlorohydrin in excess (relative to the mPEO<sub>z</sub>). (2) The reaction has to be carried out under argon atmosphere using anhydrous reactants to ensure that the precipitation of the formed NaCl in THF is quantitatively [56]. Furthermore, the absence of H<sub>2</sub>O prohibits the formation of nucleophilic OH<sup>−</sup>-ions, which would also compete with the formed mPEO<sub>z</sub> alcoholate regarding the reaction with epichlorohydrin.

By the use of EmPEO<sub>1.9</sub>, different BCPs with constant PEO<sub>1.9</sub> block size were synthesized, using this universally applicable and simplified synthesis method, by systematically varying the  $M_n$  of their PI<sub>x</sub> and PS<sub>y</sub> blocks (cf. Scheme 1), namely PI<sub>6.8</sub>PS<sub>17.3</sub>AmPEO<sub>1.9</sub>, PI<sub>14.6</sub>PS<sub>34.8</sub>AmPEO<sub>1.9</sub>, PI<sub>24.8</sub>PS<sub>25.0</sub>AmPEO<sub>1.9</sub>, PI<sub>35.1</sub>PS<sub>14.8</sub>AmPEO<sub>1.9</sub> and PI<sub>26.1</sub>PS<sub>67.3</sub>AmPEO<sub>1.9</sub> (cf. Scheme 4). While the  $M_{n,total}$  of the BCP and thus the PEO<sub>1.9</sub> block fraction remained constant, the  $M_{n,PI_x}/M_{n,PS_y}$  was varied (cf. Scheme 1a). According to this, for PI<sub>24.8</sub>PS<sub>25.0</sub>AmPEO<sub>1.9</sub> the  $M_{n,PI_x}$  is equal to the  $M_{n,PS_y}$ , in the case of PI<sub>35.1</sub>PS<sub>14.8</sub>AmPEO<sub>1.9</sub> the  $M_{n,PI_x}$  is doubled compared to the  $M_{n,PS_y}$ , whereas for PI<sub>14.6</sub>PS<sub>34.8</sub>AmPEO<sub>1.9</sub> the  $M_{n,PS_y}$  is two times larger than the  $M_{n,PI_x}$ , which is exactly the opposite compared to PI<sub>35.1</sub>PS<sub>14.8</sub>AmPEO<sub>1.9</sub>.

In addition, by keeping a  $M_{n,PI_x}/M_{n,PS_y}$  constant, in which the  $M_{n,PS_y}$  is doubled compared to the  $M_{n,PI_x}$ , the PEO<sub>1.9</sub> block proportion was varied by changing the  $M_{n,total}$  of the BCP (cf. Scheme 1b). Therefore, by halving the  $M_{n,total}$  of PI<sub>14.6</sub>PS<sub>34.8</sub>AmPEO<sub>1.9</sub>, the PEO<sub>1.9</sub> block fraction was doubled in PI<sub>6.8</sub>PS<sub>17.3</sub>AmPEO<sub>1.9</sub>. In contrast, for PI<sub>26.1</sub>PS<sub>67.3</sub>AmPEO<sub>1.9</sub>

the  $M_{n,\text{total}}$  was varied exactly in the opposite way, i.e., the  $M_{n,\text{total}}$  of  $\text{PI}_{14.6}\text{PS}_{34.8}\text{AmPEO}_{1.9}$  was doubled, resulting in a reduced  $\text{PEO}_{1.9}$  block proportion.

## Block weight ratio



**Scheme 4.** Comparison of the block weight ratio of the prepared  $\text{PI}_x\text{PS}_y\text{AmPEO}_{1.9}$ , which are systematically and independently varied with constantly always the same  $\text{PEO}_{1.9}$  block size. The polymer chain length of each block is shown in relation to the theoretical  $M_{n,\text{calc}}$  calculated from the ratio of the used masses of monomers to initiator (cf. Table 1).

### 3.3. NMR Characterization

#### 3.3.1. EmPEO<sub>1.9</sub>

First, the  $\text{EmPEO}_{1.9}$  obtained from the functionalization reaction of  $\text{mPEO}_{1.9}$  (Scheme 3) was analyzed for its quality via <sup>1</sup>H- and <sup>13</sup>C-NMR to verify that the end group modification was quantitative as required. The <sup>1</sup>H-NMR spectrum of  $\text{EmPEO}_{1.9}$  (Figure 1) shows the proton and satellite peaks (highlighted by the grey box) from the polyether chain in the chemical shift region of  $\delta = 3.4\text{--}3.7$  ppm (c in orange circle) [51,52]. The sharp singlet at  $\delta = 3.3$  ppm (d in grey circle) can be assigned to the three protons of the terminal methoxy group [51,52]. The three protons of the epoxide group attached by functionalization reaction split into three characteristic signals located at  $\delta = 2.5$  ppm (a in blue circle),  $\delta = 2.7$  ppm (a' in blue circle) and  $\delta = 3.1$  ppm (b in yellow circle) [51,52]. The integrals of these three signals are equal and have a value of one with respect to the three protons of the terminal methoxy group, indicating that the attachment of the epoxide group took place quantitatively.

The comparison of the <sup>13</sup>C-NMR spectra of  $\text{mPEO}_{1.9}$  and  $\text{EmPEO}_{1.9}$  (Figure 2) highlights the characteristic carbon signal changes due to the modification reaction (cf. for entire spectrum of  $\text{mPEO}_{1.9}$  Figure S4 and  $\text{EmPEO}_{1.9}$  Figure S2). For  $\text{mPEO}_{1.9}$  (Figure 2a), the carbon atom signal at  $\delta = 61.7$  ppm (a in dark blue circle) corresponds to the carbon atom directly linked to the OH-group and the signal at  $\delta = 72.5$  ppm to its directly adjacent carbon atom (b in yellow circle). Both carbon atom signals are not detected in the <sup>13</sup>C-NMR spectrum of the  $\text{EmPEO}_{1.9}$  (Figure 2b), confirming that the functionalization of all OH-groups with epoxide groups to form  $\text{EmPEO}_{1.9}$  is quantitatively [51]. The carbon atoms of the polyether chain at  $\delta = 70.5$  ppm (c in orange circle) and the terminal methoxy group at  $\delta = 59.0$  ppm (e in light green circle) are not affected during the modification reaction, thus the respective signals can be found in both <sup>13</sup>C-NMR spectra [51]. In contrast to the <sup>13</sup>C-NMR

spectrum of mPEO<sub>1,9</sub> (Figure 2a), two carbon atom signals appear at  $\delta = 44.1$  ppm (f in light blue circle) and  $\delta = 50.7$  ppm (g in brown circle) in <sup>13</sup>C-NMR spectrum of EmPEO<sub>1,9</sub> (Figure 2b) which are characteristic for the attached epoxide group [51].

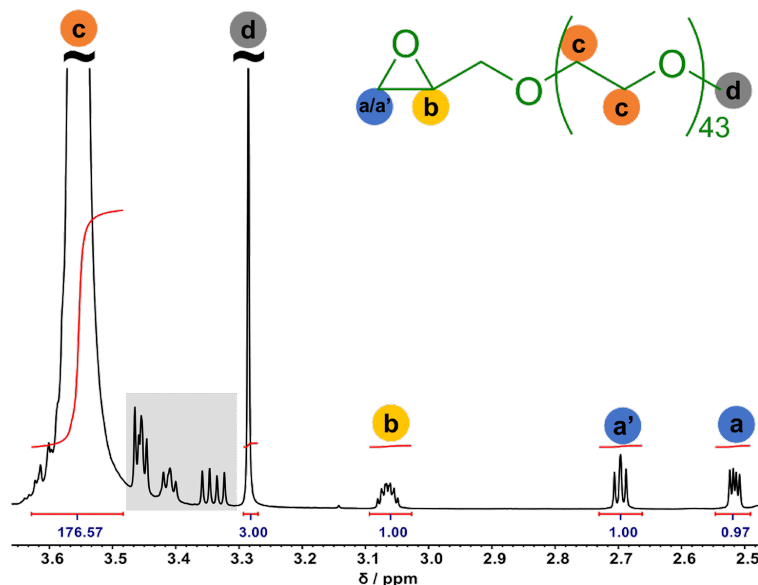


**Figure 1.** <sup>1</sup>H-NMR spectrum of the reaction product EmPEO<sub>1,9</sub> obtained by the functionalization reaction of mPEO<sub>1,9</sub> with epichlorohydrin (Scheme 3). The integrated signals indicate a quantitative formation of EmPEO<sub>1,9</sub>. The protons of the bridging CH<sub>2</sub>-group (between epoxide group and the polyether chain) as well as the satellite signals of the polyether chain are highlighted by the grey box.

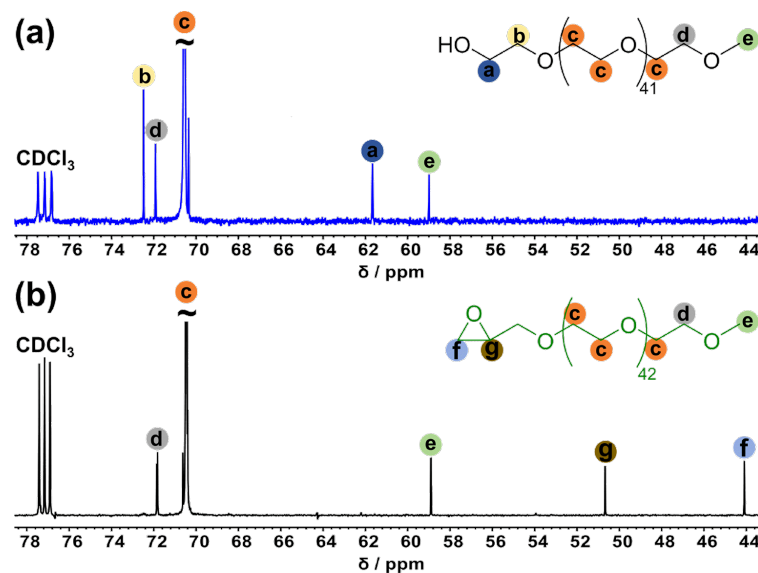


**Figure 2.** (a) <sup>13</sup>C-NMR spectrum of mPEO<sub>1,9</sub> and (b) of EmPEO<sub>1,9</sub>. The absence of signals a and b in <sup>13</sup>C-NMR spectrum of EmPEO<sub>1,9</sub> indicates the quantitative formation. For better clarity, the most intense signal (marked by c in filled orange circle) was cut off, symbolized by inserted tilde.

The successful and quantitative attachment of the epoxide group to the mPEO<sub>1,9</sub> molecule was verified by the integrals in <sup>1</sup>H-NMR as well as the altered signals in <sup>13</sup>C-NMR. Furthermore, the absence of additional signals in the <sup>1</sup>H- and <sup>13</sup>C-NMR spectra of EmPEO<sub>1,9</sub> (Figures 1 and 2b) indicated that during the modification reaction, no side reaction occurred, and no impurities were introduced (cf. Figures S1 and S2 for entire spectrum).

### 3.3.2. $\text{PI}_x\text{PS}_y\text{AmPEO}_{1,9}$

The quantitatively epoxy-functionalized  $\text{EmPEO}_{1,9}$  was used for the synthesis of different  $\text{PI}_x\text{PS}_y\text{AmPEO}_{1,9}$ , which were subsequently characterized by  $^1\text{H-NMR}$  measurements. In the following,  $\text{PI}_{14,6}\text{PS}_{34,8}\text{AmPEO}_{1,9}$  is discussed exemplarily based on its  $^1\text{H-NMR}$  result, whereas in Figure S10 and Table S1, the results of all synthesized  $\text{PI}_x\text{PS}_y\text{AmPEO}_{1,9}$  are summarized, while the individual spectra are depicted in Figures S5–S9.

The  $^1\text{H-NMR}$  spectrum of  $\text{PI}_{14,6}\text{PS}_{34,8}\text{AmPEO}_{1,9}$  is displayed in Figure 3. The signals in the range of  $\delta = 7.4$ – $6.2$  ppm can be assigned to the five aromatic protons of the phenyl group of  $\text{PS}_{34,8}$  block (red circles). The signal of the olefinic proton from the 1,4- $\text{PI}_{14,6}$  block (blue circle) is located at  $\delta = 5.2$  ppm and the two terminal protons of the 3,4- $\text{PI}_{14,6}$  block (blue circle) are located at  $\delta = 4.8$  and 4.7 ppm, respectively [57]. The integral ratio of the 1,4- $\text{PI}_{14,6}$  block to the 3,4- $\text{PI}_{14,6}$  block is 1.00: 0.15, being the same for all prepared  $\text{PI}_x\text{PS}_y\text{AmPEO}_{1,9}$  [57]. The protons of the polyether chain of the  $\text{AmPEO}_{1,9}$  (dark green circle) are localized at  $\delta = 3.7$  ppm. The signal at  $\delta = 3.4$  ppm can be attributed to the terminal methoxy group of  $\text{AmPEO}_{1,9}$  (light green circle), and the alkyl backbone protons of the entire  $\text{PI}_{14,6}\text{PS}_{34,8}\text{AmPEO}_{1,9}$  (light grey circles) are located in the range of  $\delta = 2.3$ – $1.3$  ppm. The fact that the proton signals from  $\text{AmPEO}_{1,9}$  are still present after the purification procedure of  $\text{PI}_{14,6}\text{PS}_{34,8}\text{AmPEO}_{1,9}$  indicates that  $\text{AmPEO}_{1,9}$  was covalently linked to the  $\text{PI}_{14,6}\text{PS}_{34,8}^-$  anion by a nucleophilic attack on the epoxide group of  $\text{EmPEO}_{1,9}$ , as described previously (cf. Scheme 2II). The nonbonded  $\text{EmPEO}_{1,9}$  was removed during the purification procedure because it dissolves in MeOH, which is used in the purification process [58].

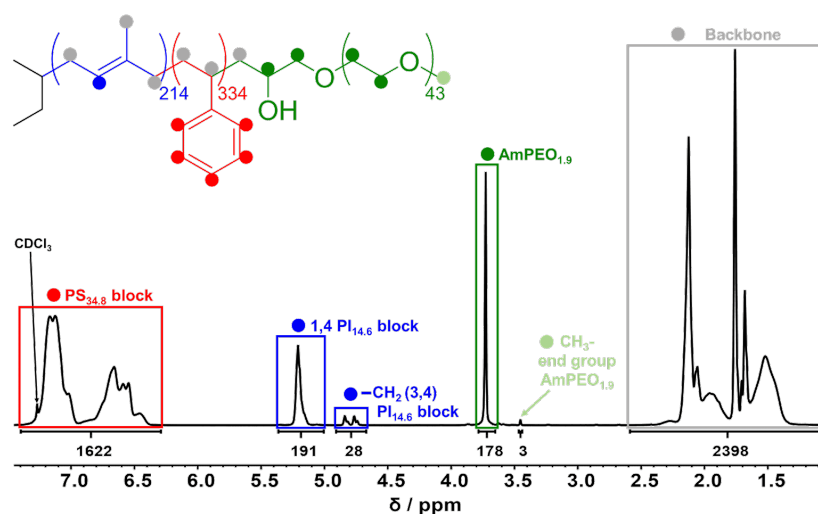


**Figure 3.**  $^1\text{H-NMR}$  spectrum of the  $\text{PI}_{14,6}\text{PS}_{34,8}\text{AmPEO}_{1,9}$  obtained by the synthesis route with  $\text{EmPEO}_{1,9}$  (Scheme 2) after precipitation and drying. The presence of the  $\text{AmPEO}_{1,9}$  proton signals after purification procedure indicates that the  $\text{AmPEO}_{1,9}$  was covalently attached to the  $\text{PI}_{14,6}\text{PS}_{34,8}^-$  anion. The integral of the protons fit to the theoretical molar mass ( $M_{n,\text{calc.}}$ ) of the individual blocks, which implies 100% reaction efficiency. The protons of the butyl group (shown in the structural formula, originating from the *sec*-BuLi) were not displayed in the spectrum for a better overview.

The theoretical molar mass ( $M_{n,\text{calc.}}$ ) of the individual blocks shown in Table 2, which was calculated from the ratio of the used masses of monomers (isoprene and styrene) to *sec*-BuLi (initiator) (cf. Table 1), fit to the respective  $^1\text{H-NMR}$  integrals of the characteristic protons from the  $\text{PI}_x$ ,  $\text{PS}_y$  and  $\text{AmPEO}_{1,9}$  blocks for all synthesized  $\text{PI}_x\text{PS}_y\text{AmPEO}_{1,9}$  (Table 3, Figure S10, Table S1).

**Table 2.** Theoretical constitutional repeating units ( $CRU_{calc.}$ ) and molar masses ( $M_{n,calc.}$ ) of the individual blocks from the synthesized  $PI_xPS_yAmPEO_{1.9}$ , calculated from the ratio of the used masses of monomers to initiator (cf. Table 1).

Polymer	$M_{n,calc.}$ /kg mol <sup>-1</sup>	$PI_x$ $CRU_{calc.}$	$M_{n,calc,PIx}$ /kg mol <sup>-1</sup>	$PS_y$ $CRU_{calc.}$	$M_{n,calc,PSy}$ /kg mol <sup>-1</sup>	$PEO_{1.9}$ $CRU_{calc.}$	$M_{n,calc,PEO1.9}$ /kg mol <sup>-1</sup>
$PI_{6.8}PS_{17.3}AmPEO_{1.9}$	26.0	100	6.8	166	17.3	43	1.9
$PI_{14.6}PS_{34.8}AmPEO_{1.9}$	51.3	214	14.6	334	34.8	43	1.9
$PI_{24.8}PS_{25.0}AmPEO_{1.9}$	51.7	365	24.8	240	25.0	43	1.9
$PI_{35.1}PS_{14.8}AmPEO_{1.9}$	51.8	516	35.1	142	14.8	43	1.9
$PI_{26.1}PS_{67.3}AmPEO_{1.9}$	95.3	384	26.1	646	67.3	43	1.9

**Table 3.** Practical constitutional repeating units ( $CRU_{NMR}$ ) and molar masses ( $M_{n,NMR}$ ) of the individual polymer blocks from the synthesized  $PI_xPS_yAmPEO_{1.9}$  determined from the respective protons number of <sup>1</sup>H-NMR integrals.

Polymer	$M_{n,NMR}$ /kg mol <sup>-1</sup>	$PI_x$ $CRU_{NMR}$	$M_{n,NMR,PIx}$ /kg mol <sup>-1</sup>	$PS_y$ $CRU_{NMR}$	$M_{n,NMR,PSy}$ /kg mol <sup>-1</sup>	$PEO_{1.9}$ $CRU_{NMR}$	$M_{n,NMR,PEO1.9}$ /kg mol <sup>-1</sup>
$PI_{6.8}PS_{17.3}AmPEO_{1.9}$	26.8	101	6.9	174	18.1	42	1.9
$PI_{14.6}PS_{34.8}AmPEO_{1.9}$	49.7	206	14.0	324	33.8	44	1.9
$PI_{24.8}PS_{25.0}AmPEO_{1.9}$	49.7	346	23.6	231	24.1	45	2.0
$PI_{35.1}PS_{14.8}AmPEO_{1.9}$	49.6	489	33.3	137	14.3	45	2.0
$PI_{26.1}PS_{67.3}AmPEO_{1.9}$	106.2	460	31.3	702	73.1	41	1.8

Considering the fact that the molar masses ( $M_{n,NMR}$ ) of the individual blocks shown in Table 3 determined from the respective proton number of <sup>1</sup>H-NMR integrals (cf. Table S1) agree with the corresponding  $M_{n,calc.}$  indicates a nearly stoichiometric conversion of the utilized masses listed in Table 1 to the desired  $PI_xPS_yAmPEO_{1.9}$  without any side reactions. This close to quantitative polymerization process is due to the high reaction control by living anionic polymerization, the controlled synthesis conditions and the use of a slight excess of the  $EmPEO_{1.9}$  during the polymer synthesis. The slight excess (10%) of  $EmPEO_{1.9}$  ensures that all  $PI_xPS_y^-$  anions are stoichiometrically saturated with the corresponding  $AmPEO_{1.9}$  blocks, whereby the chosen epoxide end group modification ensures that not more than one  $EmPEO_{1.9}$  molecule can be covalently attached per  $PI_xPS_y^-$  anion (cf. Scheme 2 and Scheme S1). Therefore, the excess of unattached  $EmPEO_{1.9}$  was removed during the purification process. In addition, the strong O-Li-ion pair acts as a kind of protecting group, avoiding unwanted crosslinking, side and termination reactions.

### 3.4. GPC Measurements

The GPC measurements were conducted to determine the molar mass ( $M_{n,GPC}$ ), to confirm the  $M_{n,NMR}$  results, the efficiency of the polymer synthesis and to determine the  $\mathcal{D}$  of the  $EmPEO_{1.9}$  as well as the synthesized  $PI_xPS_yAmPEO_{1.9}$ . The corresponding GPC traces are shown in Figure 4, and Table 4 lists the results (cf. Figures S11–S15 for the complete traces). From the GPC traces, it can be seen that all synthesized  $PI_xPS_yAmPEO_{1.9}$  polymers and  $EmPEO_{1.9}$  have a narrow, unimodal shape and as a result, a  $\mathcal{D}$  smaller than 1.10. These are:  $PI_{6.8}PS_{17.3}AmPEO_{1.9}$  ( $\mathcal{D} = 1.02$ ),  $PI_{14.6}PS_{34.8}AmPEO_{1.9}$  ( $\mathcal{D} = 1.02$ ),  $PI_{24.8}PS_{25.0}AmPEO_{1.9}$  ( $\mathcal{D} = 1.03$ ),  $PI_{35.1}PS_{14.8}AmPEO_{1.9}$  ( $\mathcal{D} = 1.03$ ),  $PI_{26.1}PS_{67.3}AmPEO_{1.9}$  ( $\mathcal{D} = 1.08$ ) with an additional minor signal, and in comparison,  $EmPEO_{1.9}$  ( $\mathcal{D} = 1.03$ ). Moreover, it can be clearly observed by the overlapping of the traces that the  $M_{n,GPC}$  of  $PI_{14.6}PS_{34.8}AmPEO_{1.9}$ ,  $PI_{24.8}PS_{25.0}AmPEO_{1.9}$  and  $PI_{35.1}PS_{14.8}AmPEO_{1.9}$  are almost identical and in the range of  $M_{n,GPC} = 62.4$ – $65.3$  kg mol<sup>-1</sup>, whereas the  $M_{n,GPC}$  of  $PI_{6.8}PS_{17.3}AmPEO_{1.9}$  is shifted to a lower value at  $M_{n,GPC} = 31.2$  kg mol<sup>-1</sup> and for  $PI_{26.1}PS_{67.3}AmPEO_{1.9}$  to a higher value at  $M_{n,GPC} = 107.6$  kg mol<sup>-1</sup>, which corresponds to their respective  $M_{n,calc.}$  and  $M_{n,NMR}$  (cf. Figure 4, Table 4). The deviation towards higher molar mass in the  $M_{n,GPC}$  compared to the  $M_{n,NMR}$  values is attributed to the fact that the GPCs used polystyrene calibration

standards. Furthermore, the GPC trace of EmPEO<sub>1.9</sub> with  $M_{n, GPC} = 2.8 \text{ kg mol}^{-1}$  shows a very narrow chain length distribution of  $\mathcal{D} = 1.03$ . Thus, it was successfully characterized prior to linkage, showing a major advantage over the short PEO<sub>z</sub> block control.

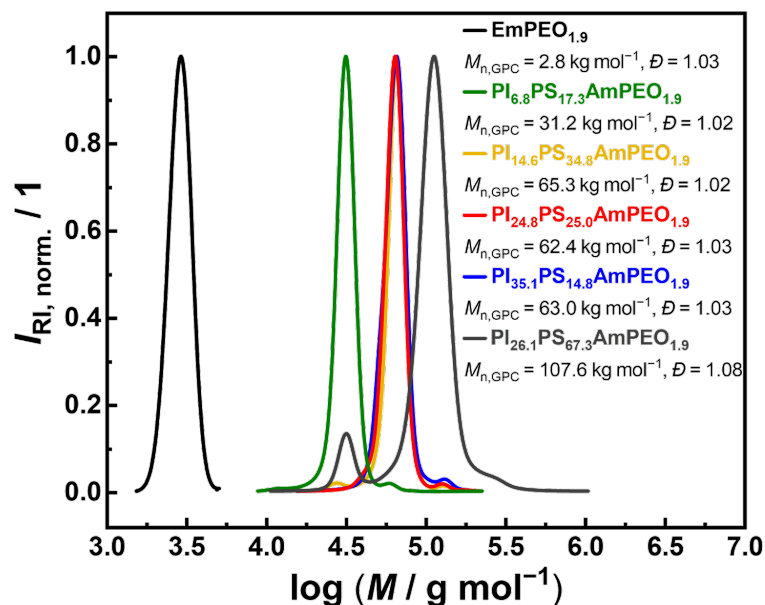


**Figure 4.** GPC traces of EmPEO<sub>1.9</sub> as well as of the synthesized PI<sub>x</sub>PS<sub>y</sub>AmPEO<sub>1.9</sub> polymers after the linkage of EmPEO<sub>1.9</sub>. The same narrow signal shape of all synthesized PI<sub>x</sub>PS<sub>y</sub>AmPEO<sub>1.9</sub> as well as of the EmPEO<sub>1.9</sub> indicate their nearly monodisperse polymer chain lengths ( $\mathcal{D} \leq 1.08$ ). For PI<sub>26.1</sub>PS<sub>67.3</sub>AmPEO<sub>1.9</sub>, a very small additional signal was detected.

**Table 4.** Overview of the theoretical molar mass ( $M_{n, calc.}$ ), the molar mass determined via <sup>1</sup>H-NMR measurement ( $M_{n, NMR}$ ) and the molar mass obtained from GPC measurement ( $M_{n, GPC}$ ) as well as the dispersity ( $\mathcal{D}$ ) of EmPEO<sub>1.9</sub> and the different synthesized PI<sub>x</sub>PS<sub>y</sub>AmPEO<sub>1.9</sub> polymers.

Polymer	$M_{n, calc.}$ <sup>1</sup> /kg mol <sup>-1</sup>	$M_{n, NMR}$ <sup>2</sup> /kg mol <sup>-1</sup>	$M_{n, GPC}$ <sup>3</sup> /kg mol <sup>-1</sup>	$\mathcal{D}$ <sup>3</sup>
EmPEO <sub>1.9</sub>	1.9	2.0	2.8	1.03
PI <sub>6.8</sub> PS <sub>17.3</sub> AmPEO <sub>1.9</sub>	26.0	26.8	31.2	1.02
PI <sub>14.6</sub> PS <sub>34.8</sub> AmPEO <sub>1.9</sub>	51.3	49.7	65.3	1.02
PI <sub>24.8</sub> PS <sub>25.0</sub> AmPEO <sub>1.9</sub>	51.7	49.7	62.4	1.03
PI <sub>35.1</sub> PS <sub>14.8</sub> AmPEO <sub>1.9</sub>	51.8	49.6	63.0	1.03
PI <sub>26.1</sub> PS <sub>67.3</sub> AmPEO <sub>1.9</sub>	95.3	106.2	107.6	1.08

<sup>1</sup> Calculated from the ratio of the used masses of monomers to initiator (cf. Table 2). <sup>2</sup> Determined from the respective proton number of <sup>1</sup>H-NMR integrals (cf. Figure S10, Table S1). <sup>3</sup> Determined by GPC measurement in THF using polystyrene standards (cf. Figure 4).

By linking the PEO<sub>z</sub> block via EmPEO<sub>z</sub>, it prevents unwanted chain termination caused by the introduction of impurities, which has a considerable influence on  $\mathcal{D}$ .

The result that the  $\mathcal{D}$  values are close to one ( $\mathcal{D} \leq 1.08$ ) indicates that the synthesized PI<sub>x</sub>PS<sub>y</sub>AmPEO<sub>z</sub> polymer chains have nearly the same length, which means that there are almost no chain terminations during the polymerization process. This is consistent with the <sup>1</sup>H-NMR results that the polymerization process is nearly quantitative and thus  $M_{n, calc.} = M_{n, NMR}$ . Therefore, this simplified polymerization procedure allows a fast and efficient polymer synthesis of tailored PI<sub>x</sub>PS<sub>y</sub>AmPEO<sub>z</sub> BCPs in a controlled and reproducible way.

### 3.5. Thermal Analysis

The synthesized  $\text{PI}_x\text{PS}_y\text{AmPEO}_{1.9}$  polymers were analyzed by DSC (cf. Figure 5a). Besides the thermal induced phase transitions, these measurements were carried out in order to obtain relevant information regarding the microphase separation.

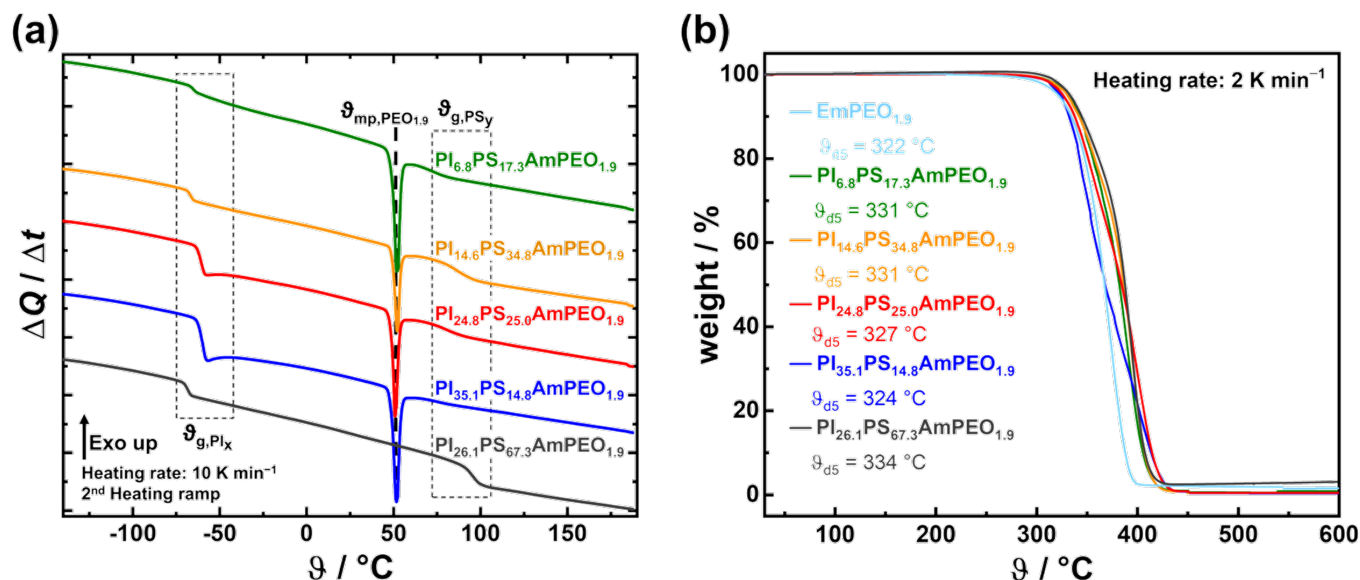


**Figure 5.** (a) DSC measurements of the synthesized  $\text{PI}_x\text{PS}_y\text{AmPEO}_{1.9}$  polymers, which show that they are microphase-separated as proven by the distinct  $\theta_g$  (glass transition temperature) of the  $\text{PI}_x$  and  $\text{PS}_y$  phase as well as the  $\theta_{\text{mp}}$  (melting point) of the  $\text{PEO}_{1.9}$  phase. An exception is  $\text{PI}_{26.1}\text{PS}_{67.3}\text{AmPEO}_{1.9}$ , where the  $\theta_{\text{mp,PEO}_{1.9}}$  is not detected. (b) TGA curves of the  $\text{EmPEO}_{1.9}$  and the synthesized  $\text{PI}_x\text{PS}_y\text{AmPEO}_{1.9}$  BCPs and their respective decomposition temperature at 5% weight loss ( $\theta_{d5}$ ).

The occurrence of the three characteristic thermal phase transitions, i.e., the glass transition temperature ( $\theta_g$ ) for the  $\text{PI}_x$  phase  $\theta_{g,\text{PI}_x}$  in the range of  $-68$  to  $-60$  °C, the  $\theta_{g,\text{PS}_y}$  for the  $\text{PS}_y$  phase in the range of  $75$  to  $96$  °C, as well as the melting point  $\theta_{\text{mp,PEO}_{1.9}}$  of the  $\text{PEO}_{1.9}$  (from  $\text{AmPEO}_{1.9}$ ) at  $\sim 50$  °C (cf. Figure S16 for DSC measurement of pure  $\text{EmPEO}_{1.9}$ ), evidence a microphase separation of the synthesized  $\text{PI}_x\text{PS}_y\text{AmPEO}_{1.9}$  BCPs (Table 5) [59]. The existence of  $\theta_{\text{mp,PEO}_{1.9}}$  indicates the phase separation of the  $\text{PEO}_{1.9}$  block from both nonpolar blocks. An exception is  $\text{PI}_{26.1}\text{PS}_{67.3}\text{AmPEO}_{1.9}$ , where the  $\theta_{\text{mp,PEO}_{1.9}}$  is not detected. The reason for the absence of the ordered crystalline structure of the  $\text{PEO}_{1.9}$  chains in  $\text{PI}_{26.1}\text{PS}_{67.3}\text{AmPEO}_{1.9}$  can be attributed either to their low content of 1.7 wt.% or to the minimal contamination, which was detected in GPC measurement, so that the entire  $\text{PEO}_{1.9}$  block is amorphous. Moreover, the two  $\theta_g$  and the  $\theta_{\text{mp,PEO}_{1.9}}$  are equal to those of the pure polymer blocks, and the absence of additional  $\theta_g$  and  $\theta_{\text{mp}}$  suggests the exclusion of any mixing of the individual blocks even at the phase boundaries. In consequence of the high tendency of phase separation (affected by the nearly monodisperse polymer chain lengths ( $D \leq 1.08$ )), a correlation between the chain length of the individual polymer blocks and the respective  $\theta_g$  is observed. An increase of the block length, which corresponds to a higher  $M_n$  of the corresponding polymer block, leads to a shift of the  $\theta_g$  to higher temperature; for instance, an increase in  $M_{n,\text{PS}_y}$  by  $\sim 10$   $\text{kg mol}^{-1}$  leads to a  $\theta_{g,\text{PS}_y}$  temperature increase of  $\sim 5$  °C (cf. Table 5). Furthermore, the fact that there is no mixing between different polymer blocks indicates that a linear dependence of change of heat capacity  $\Delta C_p$  with the weight fraction of the respective polymer block at  $\theta_g$  is detected. For example, an increase in  $M_{n,\text{PI}_x}$  of  $\sim 20$  wt.% leads to a rise in the  $\Delta C_{p,\text{PI}_x}$  by  $\sim 0.12$   $\text{J (g K)}^{-1}$  for the  $\theta_{g,\text{PI}_x}$  (Table 5).

**Table 5.** Overview of the weight fractions (wt.%), the thermal induced phase transitions  $\vartheta_{mp}$  (melting point),  $\vartheta_g$  (glass transition temperature) and the  $\Delta C_p$  (heat capacity changes) of the individual polymer blocks well as the  $\vartheta_{d5}$  (decomposition temperature at 5% weight loss) of the different  $PI_xPS_yAmPEO_{1.9}$ .

Polymer	$PI_x$ <sup>1</sup> /wt. %	$PS_y$ <sup>1</sup> /wt. %	$PEO_{1.9}$ <sup>1</sup> /wt. %	$\vartheta_{g,PIx}$ <sup>2</sup> /°C	$\Delta C_{p,PIx}$ <sup>2</sup> /J (g K) <sup>-1</sup>	$\vartheta_{g,PSy}$ <sup>2</sup> /°C	$\Delta C_{p,PSy}$ <sup>2</sup> /J (g K) <sup>-1</sup>	$\vartheta_{mp,PEO_{1.9}}$ <sup>2</sup> /°C	$\vartheta_{d5}$ <sup>3</sup> /°C
$PI_{6.8}PS_{17.3}AmPEO_{1.9}$	25.6	67.5	6.9	−63.7	0.13	74.6	0.12	50.2	331
$PI_{14.6}PS_{34.8}AmPEO_{1.9}$	28.2	68.0	3.9	−65.9	0.14	86.8	0.24	50.6	331
$PI_{24.8}PS_{25.0}AmPEO_{1.9}$	47.5	48.5	4.0	−60.7	0.27	80.9	0.14	49.9	327
$PI_{35.1}PS_{14.8}AmPEO_{1.9}$	67.2	28.8	4.0	−60.1	0.37	76.1	0.06	49.9	324
$PI_{26.1}PS_{67.3}AmPEO_{1.9}$	29.5	68.8	1.7	−67.6	0.14	95.8	0.21	-	334

<sup>1</sup> Calculated using  $M_{n,NMR}$  (cf. Table 3). <sup>2</sup> Determined by DSC measurement (cf. Figure 5a). <sup>3</sup> Determined by TGA measurement (cf. Figure 5b).

In Figure 5b, the decomposition temperature at a weight loss of 5% ( $\vartheta_{d5}$ ) of  $EmPEO_{1.9}$  and the synthesized  $PI_xPS_yAmPEO_{1.9}$  polymers as determined by TGA measurements are shown. The  $\vartheta_{d5}$  values are similar and independent of the polymer composition, with a slight trend of decreasing  $\vartheta_{d5}$  with higher  $PI_x$  content and range from 322 to 334 °C. Therefore, they have a high thermal stability for the application as polymer electrolyte templates.

### 3.6. Morphological Characterization

Based on the previous results, it is evident that this polymerization route provides precise control over the chain length distribution respectively structure on a molecular level. In the following, it is investigated how this in combination with the controlled solvent casting process affects the morphology of the membrane. In particular, the self-assembly induced highly ordered microphase separation, which was already observed from DSC measurement, is crucial for the properties of the  $PI_xPS_yAmPEO_{1.9}$  polymers and therefore plays a key role in their application. The morphology of all synthesized  $PI_xPS_yAmPEO_{1.9}$  is determined using SAXS, SEM and TEM measurements. The results of above-mentioned morphological characterizations performed on the  $PI_xPS_yAmPEO_{1.9}$  membranes are shown in Figures 6–9 and Table 6, which were controlled-cast from THF without annealing them later.

SAXS measurements were performed at room temperature on the as-cast membranes for all synthesized  $PI_xPS_yAmPEO_{1.9}$ . Figure 6 and Table 6 show the results. All of the synthesized  $PI_xPS_yAmPEO_{1.9}$  specimens exhibited strong scattering, as seen in the 2D SAXS patterns in Figure 7, Figure 8 and Figure S18, and a clear first scattering peak ( $q^*$ ), which was marked by a yellow filled circle in the SAXS curves in Figure 6, confirming the microphase separation [60,61].

In the SAXS curve of  $PI_{6.8}PS_{17.3}AmPEO_{1.9}$ , in addition to the  $q^* = 0.32 \text{ nm}^{-1}$ , additional peaks were measured at a relative peak position at  $q/q^*$  of  $\sqrt{1}$ ,  $\sqrt{3}$ ,  $\sqrt{4}$  and  $\sqrt{7}$ , indicating a HEX structure (cf. Figure 6) [18]. The same characteristic scattering peaks of a microphase-separated HEX morphology are detected for the membranes consisting of  $PI_{14.6}PS_{34.8}AmPEO_{1.9}$ ,  $PI_{35.1}PS_{14.8}AmPEO_{1.9}$  and  $PI_{26.1}PS_{67.3}AmPEO_{1.9}$ , as shown in Figure 6 [18]. However, all  $q$  values of these polymers are shifted in comparison to  $PI_{6.8}PS_{17.3}AmPEO_{1.9}$  to lower  $q$  values, whereby  $PI_{26.1}PS_{67.3}AmPEO_{1.9}$  has the lowest  $q^*$  value with  $0.11 \text{ nm}^{-1}$ . In the case of  $PI_{24.8}PS_{25.0}AmPEO_{1.9}$ , the  $q^*$  value =  $0.20 \text{ nm}^{-1}$  is the same as for  $PI_{14.6}PS_{34.8}AmPEO_{1.9}$  ( $0.20 \text{ nm}^{-1}$ ) and  $PI_{35.1}PS_{14.8}AmPEO_{1.9}$  ( $0.19 \text{ nm}^{-1}$ ). In addition to the  $q^*$  peak, further peaks at a relative position of  $q/q^*$  2 and 3 are clearly observed for  $PI_{24.8}PS_{25.0}AmPEO_{1.9}$ , indicating a LAM morphology (cf. Figure 6) [18,60].

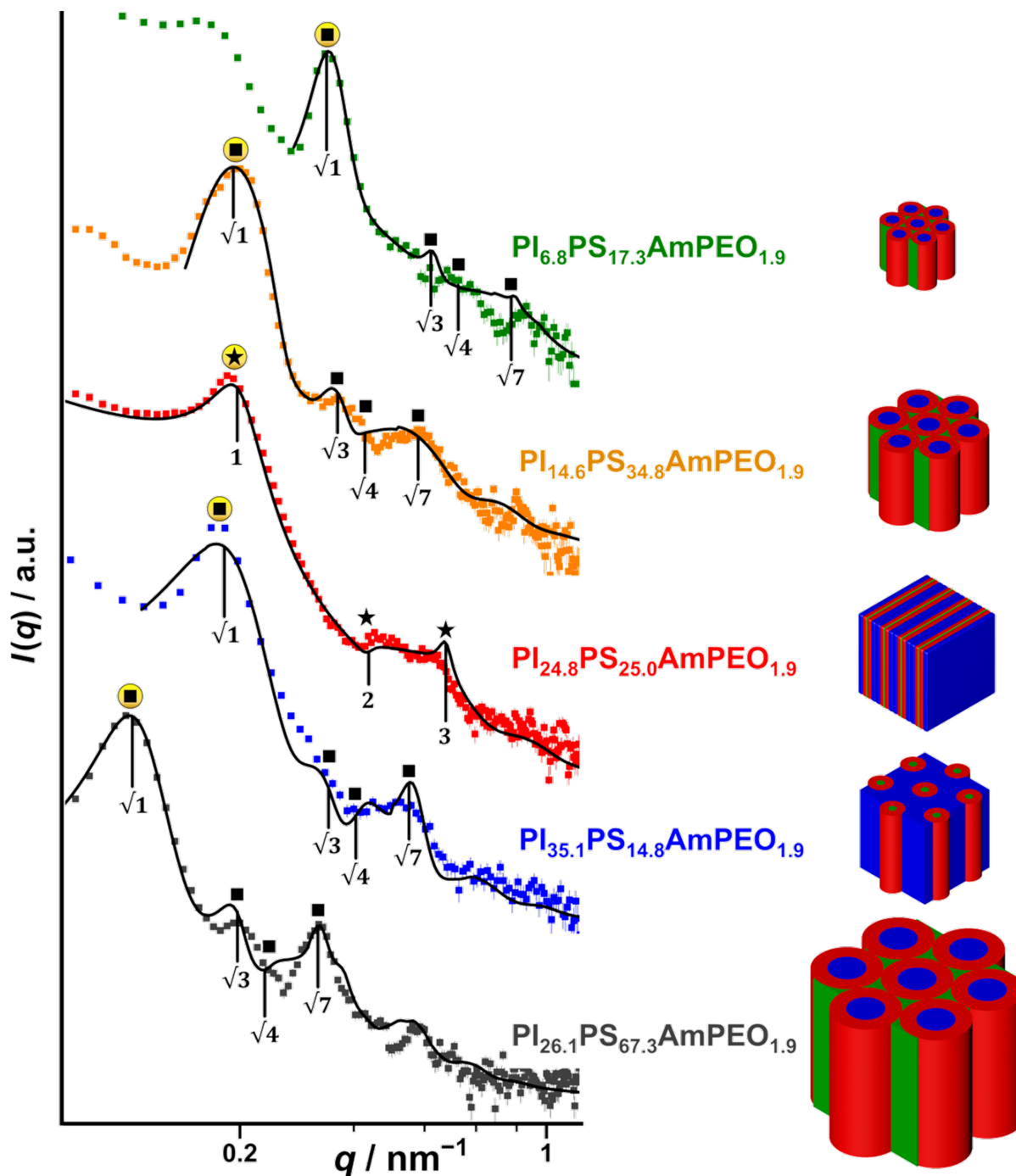


**Figure 6.** SAXS curves measured at room temperature of as-cast membranes from the synthesized  $PI_xPS_yAmPEO_{1.9}$ , by plotting the scattering intensity as a function of the magnitude of the scattering vector ( $q$ ). The first reflection peak ( $q^*$ ) determined from SAXS measurement is marked by a yellow filled circle. Black squares with the values below indicate the calculated relative peak positions at  $q/q^*$  due to hexagonally close-packed cylindrical structure and black stars indicate the respective peaks due to the lamellar structure. The theoretical fit for the morphology (black lines) and the curve obtained from SAXS measurement, as well as the calculated peak positions, match almost perfectly. On the right side are 3D drawings of the corresponding structure, therein blue represents  $PI_x$ , red  $PS_y$  and green  $PEO_{1.9}$  volume fraction and the size ratios of the drawing are equal to the average domain spacing ( $d$ ) obtained from SAXS measurement.

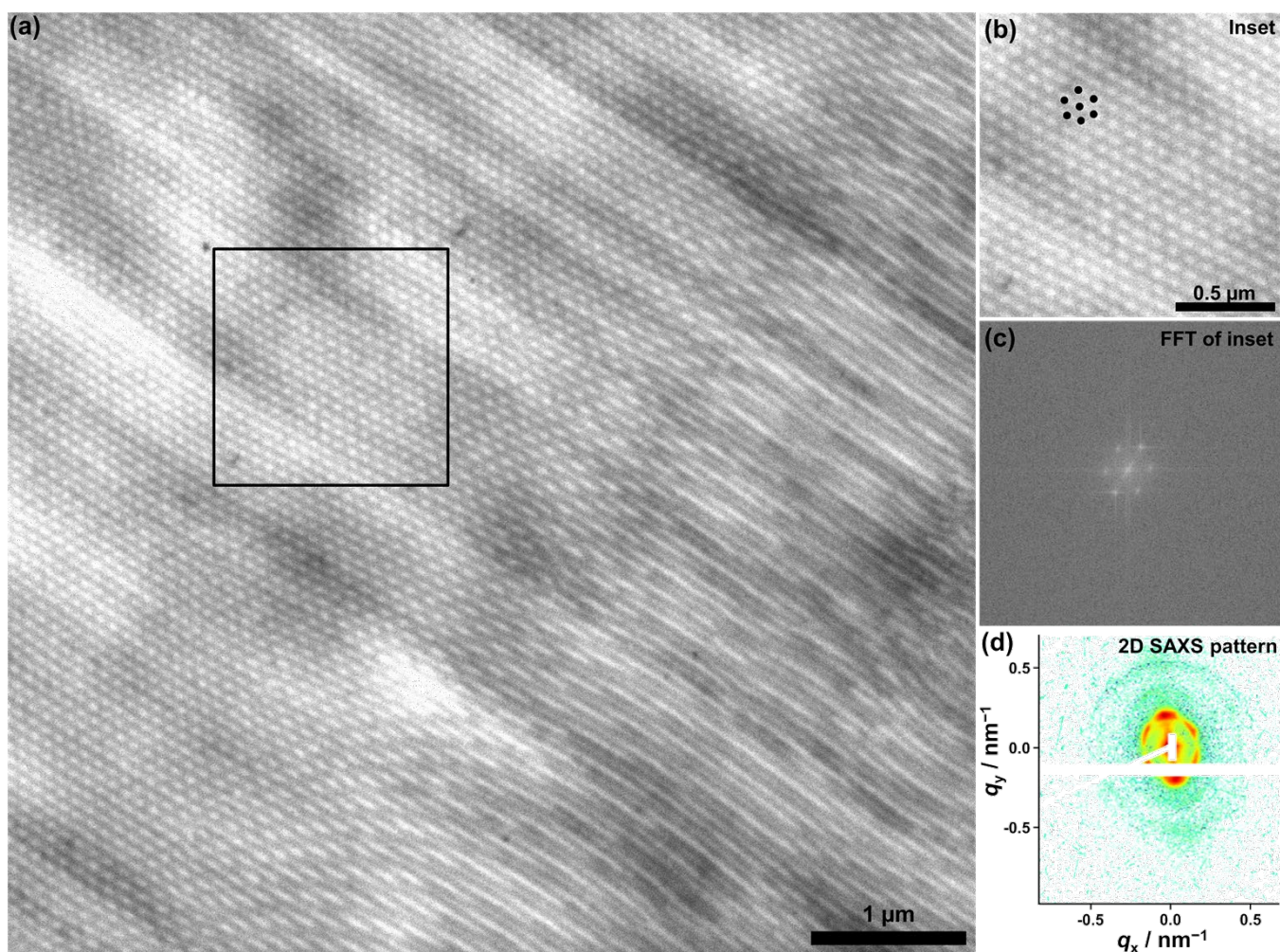


**Figure 7.** SEM images obtained at room temperature of self-assembled hexagonally close-packed cylindrical (HEX) domains in a 50 nm thick section of unstained as-cast membrane of  $\text{PI}_{14.6}\text{PS}_{34.8}\text{AmPEO}_{1.9}$  without subsequent annealing. (a) Sample overview. (b) Zoomed area of inset marked in (a). For better visibility, the hexagonal cylinder pattern of the HEX structure is marked in black as an example. (c) Two-dimensional FFT spectrum of inset area. (d) Two-dimensional SAXS pattern obtained at room temperature from the membrane in as-cast condition with a sample diameter of 2 mm.

The  $q^*$  values were used to calculate the respective average domain spacing ( $d$ ) for all  $\text{PI}_x\text{PS}_y\text{AmPEO}_{1.9}$ ; this means for a HEX structure, the distance is from cylinder to adjacent cylinder, and for a LAM structure, from center to the next center, which is listed in Table 6. In addition, from SAXS measurement of  $\text{PI}_{24.8}\text{PS}_{25.0}\text{AmPEO}_{1.9}$  the layer thickness ( $t$ ) and for samples with the HEX morphology, the cylinder radius ( $r_{\text{cylinder}}$ ) were determined and summarized in Table 6. Details concerning the fits to the radially averaged SAXS data in Figure 6 and the values in Table 6 are given in the supporting information.

The extra hump in the SAXS curve from  $\text{PI}_{6.8}\text{PS}_{17.3}\text{AmPEO}_{1.9}$  at low  $q$  value =  $0.16 \text{ nm}^{-1}$ , which therefore precedes the  $q^*$  value =  $0.32 \text{ nm}^{-1}$  and was not fitted, comes most probably from heterogeneities in the structure on length scales larger than the unit cell. The reason that only the one peak is seen and the others are suppressed lies in the ratio of  $r_{\text{cylinder}}$  and  $d$  because in this combination, the peaks fall on the minima and are suppressed.

For all investigated polymers, the  $\text{PEO}_{1.9}$  block is with a volume fraction ( $\varphi$ ) of 2–6% too small to be detected by SAXS measurements. Thus, it was not necessary to include the  $\text{PEO}_{1.9}$  block in the fit, as from DSC measurements it is known to be phase-separated from the nonpolar blocks, so a simplified diblock model was used.

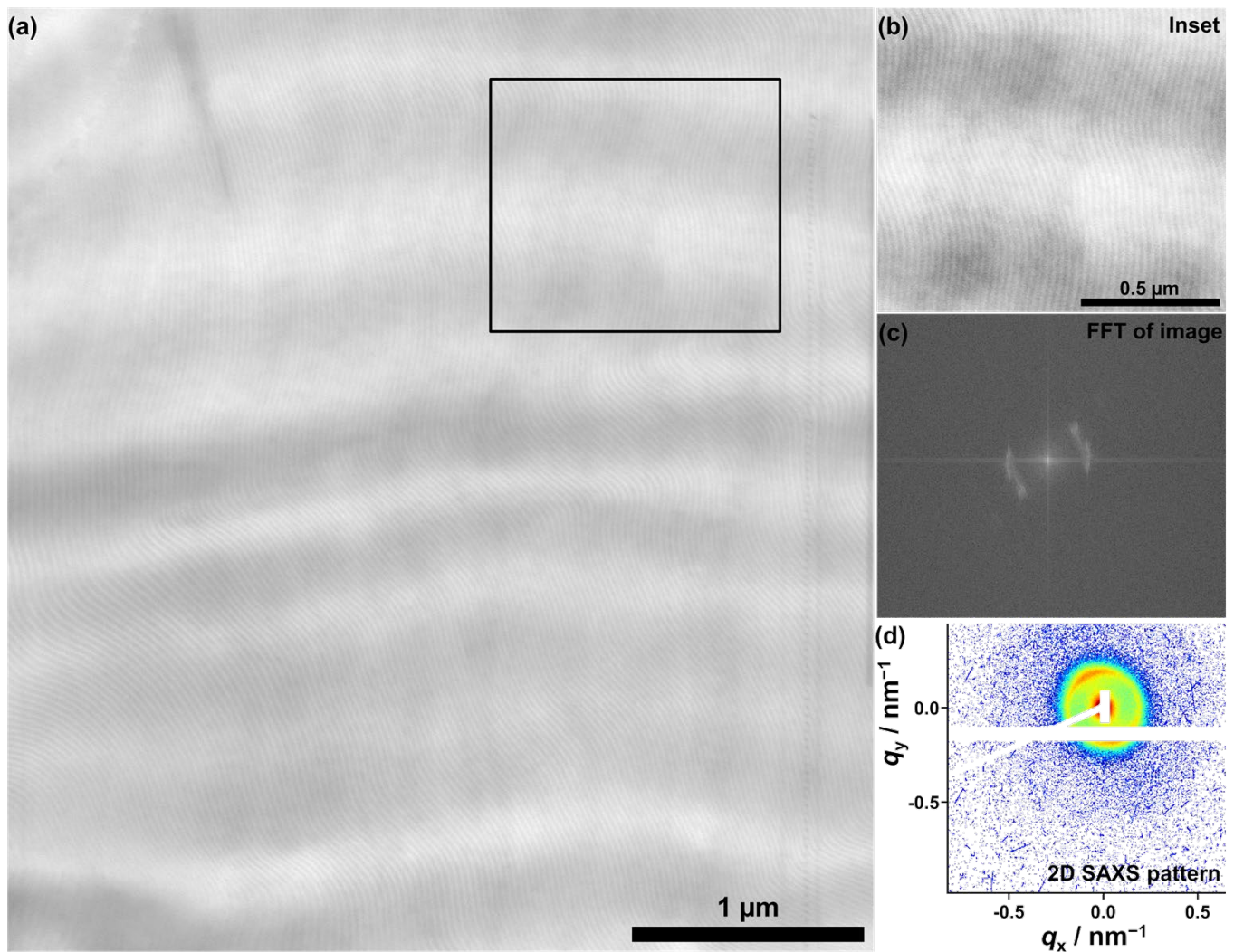


**Figure 8.** SEM images obtained at room temperature from an ultra-thin section of self-assembled lamellar domains of unstained as-cast membrane of PI<sub>24.8</sub>PS<sub>25.0</sub>AmPEO<sub>1.9</sub> without subsequent annealing. (a) Sample overview. (b) Zoomed image of area marked in the overview image in (a). (c) Two-dimensional FFT spectrum over the entire overview image (a). (d) Two-dimensional SAXS pattern obtained at room temperature from the membrane in as-cast condition with a sample diameter of 2 mm.

For all samples, the fit used to determine the morphology matches very well to the measured SAXS curve shapes (cf. plotted black line in the SAXS curves in Figure 6). Therefore, the calculated relative peak positions at  $q/q^*$  (cf. black squares for HEX and black stars for LAM structure in Figure 6) fit almost perfectly to the maxima and minima in the respective obtained SAXS curves. The model used for the fitting is either using homogenous cylinder form factor for the HEX or platelets form factor for the LAM phases. Even with this rather simple model, a precise fit of the radially averaged scattering data was achieved. The  $\varphi$  for different blocks were calculated from the ratio of  $r_{\text{cylinder}}$  or  $t$  to the fitted  $d$  and are listed in Table 6.

The  $d$  values calculated from measured  $q^*$  correlate with the total  $M_{n,\text{NMR}}$  of the PI<sub>*x*</sub>PS<sub>*y*</sub>AmPEO<sub>1.9</sub>. This means that PI<sub>6.8</sub>PS<sub>17.3</sub>AmPEO<sub>1.9</sub> possesses not only the smallest structure size with  $d = 22.4$  nm, but also the fact that it is about half of the size compared to PI<sub>14.6</sub>PS<sub>34.8</sub>AmPEO<sub>1.9</sub> with  $d = 35.7$  nm, PI<sub>24.8</sub>PS<sub>25.0</sub>AmPEO<sub>1.9</sub> with  $d = 31.7$  nm and PI<sub>35.1</sub>PS<sub>14.8</sub>AmPEO<sub>1.9</sub> with  $d = 39.2$  nm. The same behavior, but this time reversed, is seen for PI<sub>26.1</sub>PS<sub>67.3</sub>AmPEO<sub>1.9</sub>, which not only has the largest structure size with

$d = 63.6$  nm, but also its size is in comparison to  $\text{PI}_{14.6}\text{PS}_{34.8}\text{AmPEO}_{1.9}$ ,  $\text{PI}_{24.8}\text{PS}_{25.0}\text{AmPEO}_{1.9}$  and  $\text{PI}_{35.1}\text{PS}_{14.8}\text{AmPEO}_{1.9}$  about two times larger. Therefore, the structure size ratios of the different  $\text{PI}_x\text{PS}_y\text{AmPEO}_{1.9}$  to each other are in accurate accordance with their respective  $M_{n,\text{NMR}}$  (cf. Scheme 4, Table 4). Also, the measured  $r_{\text{cylinder}}$  have the same relationship to each other as the previously described  $d$  (cf. Table 6).

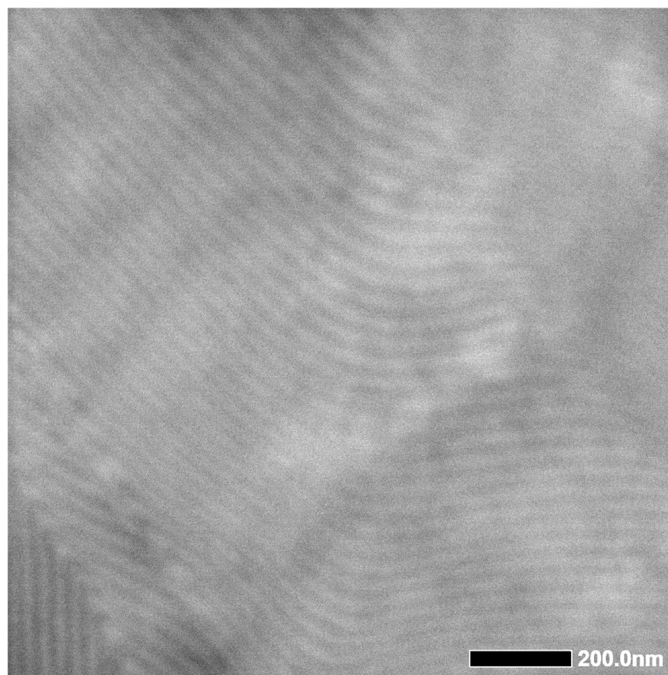


**Figure 9.** STEM image obtained at room temperature from a 50 nm thick section of self-assembled lamellar domains of an unstained as-cast membrane of  $\text{PI}_{24.8}\text{PS}_{25.0}\text{AmPEO}_{1.9}$  without subsequent annealing.

**Table 6.** Summary of SAXS results determined at room temperature of the as-cast membranes of the different  $\text{PI}_x\text{PS}_y\text{AmPEO}_{1.9}$ .

Polymer	$f_{\text{PI}_x}$ <sup>1</sup> /%	$f_{\text{PS}_y}$ <sup>1</sup> /%	$f_{\text{PEO}_{1.9}}$ <sup>1</sup> /%	$q^*$ <sup>2</sup> /nm <sup>-1</sup>	Phase <sup>3</sup>	$d$ <sup>4</sup> /nm	$r_{\text{cylinder}}$ <sup>5</sup> /nm	$\Phi_{\text{cylinder}}$ <sup>6</sup> /%	Domain Size <sup>9</sup> /nm
$\text{PI}_{6.8}\text{PS}_{17.3}\text{AmPEO}_{1.9}$	29	65	6	0.32	HEX	22.4	6.1	29 ( $\text{PI}_{6.8}$ )	90
$\text{PI}_{14.6}\text{PS}_{34.8}\text{AmPEO}_{1.9}$	32	65	3	0.20	HEX	35.7	10.4	34 ( $\text{PI}_{14.6}$ )	122
$\text{PI}_{24.8}\text{PS}_{25.0}\text{AmPEO}_{1.9}$	52	45	3	0.20	LAM	31.7	$t^7 = 16.4$	52 ( $\text{PI}_{24.8}$ ) <sub>LAM</sub> <sup>8</sup>	86
$\text{PI}_{35.1}\text{PS}_{14.8}\text{AmPEO}_{1.9}$	71	26	3	0.19	HEX	39.2	10.9	<sup>31</sup> ( $\text{PS}_{14.8}\text{AmPEO}_{1.9}$ )	63
$\text{PI}_{26.1}\text{PS}_{67.3}\text{AmPEO}_{1.9}$	33	66	2	0.11	HEX	63.6	16.9	28 ( $\text{PI}_{26.1}$ )	147

<sup>1</sup>  $f_i$  = monomer volume fraction on basis of published homopolymer densities ( $\rho_{\text{PI}_x} = 0.830$ ,  $\rho_{\text{PS}_y} = 0.969$ ,  $\rho_{\text{PEO}_z} = 1.064$  in  $\text{g cm}^{-3}$ ) [61] and calculated using  $M_{n,\text{NMR}}$  (cf. Table 3). Note that these densities were determined for 140 °C, which may cause deviations. <sup>2</sup>  $q^*$  is the position of the first scattering peak, determined by SAXS. <sup>3</sup> HEX = hexagonally close-packed cylindrical and LAM = lamella structure, determined by SAXS measurement. <sup>4</sup>  $d$  = average domain spacing. <sup>5</sup>  $r_{\text{cylinder}}$  = radius of cylinder determined by SAXS. <sup>6</sup>  $\Phi_{\text{cylinder}}$  = volume fraction of cylinder based on ratio of  $r_{\text{cylinder}}$  to  $d$ . <sup>7</sup>  $t$  = layer thickness determined by SAXS. <sup>8</sup> Volume fraction of lamella based on ratio of  $t$  to  $d$ . <sup>9</sup> Domain size = determined by SAXS.

Using the  $M_{n,\text{NMR}}$  of the individual polymer blocks (cf. Table 3) and on basis of published homopolymer densities ( $\rho_{\text{PI}_x} = 0.830$ ,  $\rho_{\text{PS}_y} = 0.969$ ,  $\rho_{\text{PEO}_z} = 1.064$  in  $\text{g cm}^{-3}$ , note that these densities were determined for 140 °C, which may cause slight deviations) [61], the monomer volume fractions ( $f_i$ ) of the  $\text{PI}_x$  block ( $f_{\text{PI}_x}$ ), the  $\text{PS}_y$  block ( $f_{\text{PS}_y}$ ) and the  $\text{PEO}_{1.9}$  block ( $f_{\text{PEO}_{1.9}}$ ) were calculated and listed in Table 6. For  $\text{PI}_{6.8}\text{PS}_{17.3}\text{AmPEO}_{1.9}$ ,  $\text{PI}_{14.6}\text{PS}_{34.8}\text{AmPEO}_{1.9}$  and  $\text{PI}_{26.1}\text{PS}_{67.3}\text{AmPEO}_{1.9}$ , the volume ratio of the  $\text{PI}_x$  block to the  $\text{PS}_y\text{AmPEO}_{1.9}$  block always remains the same and was in the range of ~29–33% for  $f_{\text{PI}_x}$

and ~68–71% for  $f_{\text{PS}_y\text{AmPEO}_{1.9}}$ . The volume fraction of the cylinder ( $\varphi_{\text{cylinder}}$ ) was equal for all with ~28–34%, which matches very well with the  $f_{\text{PI}_x}$ . Accordingly, it was obvious that they have the same HEX structure. Consequently, the cylinder from the HEX structure corresponds to the  $\text{PI}_x$  block, because the  $r_{\text{cylinder}}$  ratio of the different polymers, i.e.,  $\text{PI}_{6.8}\text{PS}_{17.3}\text{AmPEO}_{1.9}$ ,  $\text{PI}_{14.6}\text{PS}_{34.8}\text{AmPEO}_{1.9}$  and  $\text{PI}_{26.1}\text{PS}_{67.3}\text{AmPEO}_{1.9}$ , agrees exactly with the respective  $M_{n,\text{NMR},\text{PI}_x}$  ratio. As a result, the HEX structures differ from each other only in terms of size.

The volume ratio for  $\text{PI}_{35.1}\text{PS}_{14.8}\text{AmPEO}_{1.9}$  with  $f_{\text{PI}_{35.1}} = 71\%$  and  $f_{\text{PS}_{14.8}\text{AmPEO}_{1.9}} = 29\%$  is exactly the opposite compared to the previously discussed  $\text{PI}_x\text{PS}_y\text{AmPEO}_{1.9}$ . The determined  $\varphi_{\text{cylinder}}$  with 31% matches quite closely with the  $f_{\text{PS}_{14.8}\text{AmPEO}_{1.9}}$ . Consequently, the detected HEX structure fits accurately; however, due to the inverted volume fractions, a reverse phase with  $\text{PS}_{14.8}\text{AmPEO}_{1.9}$  cylinders exists. Hence,  $r_{\text{cylinder}}$  with a value of 10.9 nm corresponds to the  $M_{n,\text{NMR}}$  of  $\text{PS}_{14.8}$  and  $\text{AmPEO}_{1.9}$  block and is the same size as  $r_{\text{cylinder}}$  of  $\text{PI}_{14.6}\text{PS}_{34.8}\text{AmPEO}_{1.9}$  as well as its  $M_{n,\text{NMR}}$  of the  $\text{PI}_{14.6}$  block. This fact confirms that  $\text{PI}_{35.1}\text{PS}_{14.8}\text{AmPEO}_{1.9}$  has the reverse phase of the HEX structure of the  $\text{PI}_{14.6}\text{PS}_{34.8}\text{AmPEO}_{1.9}$ .

The measured LAM morphology for  $\text{PI}_{24.8}\text{PS}_{25.0}\text{AmPEO}_{1.9}$  with the volume ratio of  $f_{\text{PI}_{24.8}} = 52\%$  and  $f_{\text{PS}_{25.0}\text{AmPEO}_{1.9}} = 48\%$  fits exactly with the determined almost equal volume fraction of lamella ( $\varphi_{\text{LAM}}$ ) of the  $\text{PI}_{24.8}$  block with  $\varphi_{\text{LAM}} = 52\%$  and 48% for the  $\text{PS}_{25.0}\text{AmPEO}_{1.9}$  block.

Indeed, as expected from the  $\text{PI}_x\text{PS}_y$  phase diagram, the nearly symmetric  $\text{PI}_{24.8}\text{PS}_{25.0}\text{AmPEO}_{1.9}$  forms a LAM, while all other, more asymmetric  $\text{PI}_x\text{PS}_y\text{AmPEO}_{1.9}$  show a HEX morphology [18,24].

In order to visualize the previously described structures more clearly, corresponding 3D drawings were plotted based on the parameters obtained from the SAXS measurements with the assumption that the  $\text{PEO}_{1.9}$  block is fully phase-separated (cf. 3D drawings on the right site in Figure 6).

The obtained SAXS results match almost perfectly for all  $\text{PI}_x\text{PS}_y\text{AmPEO}_{1.9}$  with their respective polymer composition determined from NMR, thermal analysis and GPC measurements, and in particular, when they are compared with each other.

For all  $\text{PI}_x\text{PS}_y\text{AmPEO}_{1.9}$ , the SAXS measurement results indicate a high degree of long-range order in the structure due to the strong scattering in the respective 2D SAXS pattern, but also due to the fact that the curve shape shows a number of clear peaks that agree very well with the fit as well as with the calculated peak positions. For instance, in  $\text{PI}_{24.8}\text{PS}_{25.0}\text{AmPEO}_{1.9}$  the presence of  $2q^*$  and  $3q^*$  suggests that the LAM morphology is present with a highly long-range arrangement [60,62].

In order to determine a more detailed, local long-range order as well as the orientation of the structure, SEM measurements were carried out. In particular, these two structural parameters of the membrane are crucial for the application of BCP as a structure-giving polymer matrix in electrolyte. In addition, the structure determined from the SAXS results is also checked. For this purpose, exemplary SEM measurements were performed on unstained ultra-thin sections of about 50 to 100 nm thickness from  $\text{PI}_{14.6}\text{PS}_{34.8}\text{AmPEO}_{1.9}$  for the HEX structure and from  $\text{PI}_{24.8}\text{PS}_{25.0}\text{AmPEO}_{1.9}$  for the LAM structure. In Scheme S2, the procedure of sample preparation by cryo-ultramicrotomy as well as sample placement onto the grid is schematically shown.

Results of  $\text{PI}_{14.6}\text{PS}_{34.8}\text{AmPEO}_{1.9}$  are shown in Figure 7; the ones for  $\text{PI}_{24.8}\text{PS}_{25.0}\text{AmPEO}_{1.9}$  are displayed in Figure 8. In (a), an overview image of several  $\mu\text{m}^2$  in size is shown. The marked area in a) was enlarged as inset in b) to make the structure visible in more detail (i.e., periodic lamellae or hexagonal cylinder arrangement). In (c), the fast Fourier transformation (FFT) of the area in (a) in case of the LAM and of the inset (b) in case of the HEX structure is added to indicate the average orientation of the structure. The good contrast of the sample is achieved through the relatively low accelerating voltage of 30 kV used for STEM-imaging in the SEM. Hence, samples can be measured without staining. Additionally, in both figures under (d), the corresponding SAXS pattern is shown to compare it with the FFT spectrum.

For  $PI_{14.6}PS_{34.8}AmPEO_{1.9}$ , a long-range and highly ordered HEX structure of cylinders is clearly visible in the overview image of Figure 7a, respectively, in the enlarged inset in (b) and corresponds with the SAXS result. In particular, it is remarkable that the hexagonal cylinder pattern of the HEX structure is clearly visible and almost identical in the FFT spectrum in (c) as well as in the SAXS pattern in (d). This means that the cylinders have the same arrangement and distance to each other in the macroscopic sample volume (2 mm sample diameter in the SAXS capillaries) and in the microscopic sample area in the SEM image and are aligned straight through the entire volume. Furthermore, from the SEM image, it is evident that for the cast film HEX structure, the cylinder axes are located in plane.

In case of  $PI_{24.8}PS_{25.0}AmPEO_{1.9}$  in the large overview image in Figure 8a, respectively, in the inset in b), a long-range and highly ordered LAM structure is clearly evident, which is also consistent with the SAXS result and corroborated by the 2D FFT result. The obtained 2D FFT spectrum reveals two “beam-like shapes” according to the LAM structure going vertical through the sample (cf. Figure 8c). Also, the SAXS pattern in Figure 8d shows the two “beam-like shapes” which differ from those in the FFT nearly only by the fact that they are slightly tilted. Most likely this is due to the placement of the sample into the SAXS capillary. Considering that the FFT spectrum and the SAXS pattern look almost the same, the lamellae are microscopically as well as macroscopically equally oriented and have the same distance to each other.

Moreover, a TEM image of  $PI_{24.8}PS_{25.0}AmPEO_{1.9}$  of the unstained membrane was obtained in STEM mode. Usually, stained samples are measured [18,24,63,64]. The TEM result shown in Figure 9 displays the same LAM structure as already seen in SEM.

As a result,  $PI_{14.6}PS_{34.8}AmPEO_{1.9}$  and  $PI_{24.8}PS_{25.0}AmPEO_{1.9}$  possess a nearly perfectly ordered HEX respectively LAM structure, at least over the total SEM and TEM measurement  $\mu\text{m}$  size area as well as the 2 mm thick sample volume for the SAXS measurement. Therefore, they show an extraordinary long-range orientation. The strongly distinct microphase separation, most likely caused by the very narrow polymer chain length distribution, in combination with the controlled solution casting process ensuring enough time for self-assembly, leads to these exceptional morphological properties. These properties are crucial for an excellent polymer electrolyte matrix, because the conductive pathways and finally the  $Li^+$  transport should be aligned almost optimally to each other over an extremely long range inside the BCP membrane.

Furthermore, particularly in case of  $PI_{24.8}PS_{25.0}AmPEO_{1.9}$ , horizontal cutting artifacts can be recognized in the sample overview image as brighter and darker waves. This is a common cutting artifact of cryo-ultramicrotomy, which results from compression of the section during sectioning and extends perpendicular to the cutting direction [65]. As the cutting direction was perpendicular to the membrane and a ribbon of sections could be imaged on the grid by SEM, it is possible to determine the orientation of the lamellae within the membrane over a larger sample surface area and at several sample positions (cf. Scheme S2). The lamellae are arranged from top to bottom, i.e., vertically across the sample. Compression artefacts are perpendicular to the lamellae, indicating that the cutting direction across the membrane is the same as the orientation of the lamellae in the BCP. In other words, the lamellae are continuous aligned orthogonally to the polymer surface and therefore also at the potential use in electrolytes as a structure-giving BCP matrix to the electrode interface, i.e., connecting both electrodes to each other. It has already been shown in our patent that these BCPs can be used as a structure-giving BCP matrix in electrolytes to obtain very high ionic conductivities [43]. Such electrolytes provide comparable, and in some cases even better, ionic conductivities than those reported by Dörr and Pelz et al. [10,11,37].

#### 4. Conclusions

Herein, we introduced a convergent synthesis method based on the modular principle, which ensures the access to well-defined  $PI_xPS_yPEO_z$  linear triblock copolymers with

consistently the same very short and precise PEO<sub>z</sub> block. For this purpose, a prefabricated and commercially available mPEO<sub>z</sub> block is used, which is selectively functionalized with an epoxy end group to EmPEO<sub>z</sub>. The EmPEO<sub>z</sub> block is covalently attached to the PI<sub>x</sub>PS<sub>y</sub><sup>−</sup> anion synthesized by living anionic polymerization and thus terminated to the corresponding BCP. Thereby, by utilizing the O-Li ion pair formation between the epoxide group of the EmPEO<sub>z</sub> and the living anion, it is ensured that only a single ring-opening reaction occurs. Therefore, the handling of EO gas monomers during the BCP polymerization can be avoided.

The systematic variation of the block length reveals two major and independent influences of the polymer structure. By varying the  $M_{n,PI_x}/M_{n,PS_y}$  at a constant  $M_{n,total}$ , the morphology could be precisely controlled. Alternatively, by changing the  $M_{n,total}$  at the same  $M_{n,PI_x}/M_{n,PS_y}$ , only the PEO<sub>z</sub> block fraction could be altered and adjusted, while keeping the morphology constant.

This simplified and reproducible one-pot polymerization, with 100% reaction efficiency, obtains highly ordered PI<sub>x</sub>PS<sub>y</sub>AmPEO<sub>z</sub> BCPs whose morphology can be largely controlled within the polymer membrane on microscopic and macroscopic levels. Largely controlled means at the microscopic or molecular level that the polymer chain lengths can be precisely selected, are nearly monodisperse and the respective BCP possesses a very high degree of phase separation. Moreover, the highly uniform polymer blocks combined with the controlled solution casting process lead to PI<sub>x</sub>PS<sub>y</sub>AmPEO<sub>z</sub> membranes with a very high and exceptionally long-range ordered structure up to the mm scale.

Overall, due to the always constant PEO<sub>z</sub> block size, the high control over the order and orientation of the morphology as well as the PEO<sub>z</sub> block fraction, these BCPs are suitable for subsequent targeted investigation of their influence as a structure-giving matrix in corresponding solid polymer electrolytes with respect to Li<sup>+</sup> transport up to the macroscale level.

**Supplementary Materials:** The following supporting information can be downloaded at: <https://www.mdpi.com/article/10.3390/polym15092128/s1>, Scheme S1: Illustration of the utilization of the blocking effect for single EmPEO<sub>z</sub> chain attachment to the PI<sub>x</sub>PS<sub>y</sub><sup>−</sup> anion with Li<sup>+</sup> as counterion due to the strong O-Li affinity. Figure S1: <sup>1</sup>H-NMR spectrum of EmPEO<sub>1.9</sub>. Figure S2: <sup>13</sup>C-NMR spectrum of EmPEO<sub>1.9</sub>. Figure S3: <sup>1</sup>H-NMR spectrum of mPEO<sub>1.9</sub>. Figure S4: <sup>13</sup>C-NMR spectrum of mPEO<sub>1.9</sub>. Figure S5: <sup>1</sup>H-NMR spectrum of PI<sub>6.8</sub>PS<sub>17.3</sub>AmPEO<sub>1.9</sub>. Figure S6: <sup>1</sup>H-NMR spectrum of PI<sub>14.6</sub>PS<sub>34.8</sub>AmPEO<sub>1.9</sub>. Figure S7: <sup>1</sup>H-NMR spectrum of PI<sub>24.8</sub>PS<sub>25.0</sub>AmPEO<sub>1.9</sub>. Figure S8: <sup>1</sup>H-NMR spectrum of PI<sub>35.1</sub>PS<sub>14.8</sub>AmPEO<sub>1.9</sub>. Figure S9: <sup>1</sup>H-NMR spectrum of PI<sub>26.1</sub>PS<sub>67.3</sub>AmPEO<sub>1.9</sub>. Figure S10: Comparison of the characteristic signals in the <sup>1</sup>H-NMR spectra of the synthesized PI<sub>x</sub>PS<sub>y</sub>AmPEO<sub>1.9</sub>. Table S1: Comparison of the number of protons determined from <sup>1</sup>H-NMR integrals of the individual polymer blocks of the synthesized PI<sub>x</sub>PS<sub>y</sub>AmPEO<sub>1.9</sub>. Figure S11: Full GPC trace of PI<sub>6.8</sub>PS<sub>17.3</sub>AmPEO<sub>1.9</sub>. Figure S12: Full GPC trace of PI<sub>14.6</sub>PS<sub>34.8</sub>AmPEO<sub>1.9</sub>. Figure S13: Full GPC trace of PI<sub>24.8</sub>PS<sub>25.0</sub>AmPEO<sub>1.9</sub>. Figure S14: Full GPC trace of PI<sub>35.1</sub>PS<sub>14.8</sub>AmPEO<sub>1.9</sub>. Figure S15: Full GPC trace of PI<sub>26.1</sub>PS<sub>67.3</sub>AmPEO<sub>1.9</sub>. Figure S16: DSC measurement of EmPEO<sub>1.9</sub>. Figure S17: Exemplary photo of a colorless and transparent PI<sub>x</sub>PS<sub>y</sub>AmPEO<sub>1.9</sub> membrane cast from THF. Figure S18: Two-dimensional SAXS patterns obtained at room temperature from the membrane in as-cast condition with a sample diameter of 2 mm of the synthesized PI<sub>6.8</sub>PS<sub>17.3</sub>AmPEO<sub>1.9</sub>, PI<sub>35.1</sub>PS<sub>14.8</sub>AmPEO<sub>1.9</sub> and PI<sub>26.1</sub>PS<sub>67.3</sub>AmPEO<sub>1.9</sub>. Details concerning fits to radially averaged SAXS data. Scheme S2: Procedure of sample preparation by cryo-ultramicrotomy as well as sample placement onto the grid.

**Author Contributions:** Conceptualization, H.-D.W., M.G. and D.T.K.; validation, D.T.K.; investigation, D.T.K., S.K., V.S., A.J.B., M.D. and B.F.; resources, H.-D.W., S.F., M.W., J.M. and P.T.; writing—original draft preparation, D.T.K.; writing—review and editing, D.T.K., M.G., H.-D.W., S.F., S.K., M.D., B.F., V.S., A.J.B. and P.T.; visualization, D.T.K., M.G., S.K., B.F. and M.D.; supervision, H.-D.W., M.W. and M.G.; funding acquisition, H.-D.W., M.W. and P.T. All authors have read and agreed to the published version of the manuscript.

**Funding:** This research was funded by the German Federal Ministry of Education and Research (BMBF) within 'FestBatt' (13XP0175C), 'FestBatt 2' (03XP0429C) and 'MEET-HiEnD III' (03XP0258A).

**Data Availability Statement:** The data presented in this study are available from the corresponding authors on request.

**Conflicts of Interest:** The authors declare no conflict of interest.

## References

1. Allen, C.; Maysinger, D.; Eisenberg, A. Nano-engineering block copolymer aggregates for drug delivery. *Colloids Surf. B Biointerfaces* **1999**, *16*, 3–27. [[CrossRef](#)]
2. Adams, M.L.; Lavasanifar, A.; Kwon, G.S. Amphiphilic block copolymers for drug delivery. *J. Pharm. Sci.* **2003**, *92*, 1343–1355. [[CrossRef](#)] [[PubMed](#)]
3. Mai, Y.; Eisenberg, A. Self-assembly of block copolymers. *Chem. Soc. Rev.* **2012**, *41*, 5969–5985. [[CrossRef](#)] [[PubMed](#)]
4. Nedelcu, M.; Lee, J.; Crossland, E.J.W.; Warren, S.C.; Orilall, M.C.; Guldin, S.; Hüttner, S.; Ducati, C.; Eder, D.; Wiesner, U.; et al. Block copolymer directed synthesis of mesoporous TiO<sub>2</sub> for dye-sensitized solar cells. *Soft Matter* **2009**, *5*, 134–139.
5. Perrin, L.; Phan, T.; Querelle, S.; Deratani, A.; Bertin, D. Polystyrene-*block*-poly(ethylene oxide)-*block*-polystyrene: A New Synthesis Method Using Nitroxide-Mediated Polymerization from Poly(ethylene oxide) Macroinitiators and Characterization of the Architecture Formed. *Macromolecules* **2008**, *41*, 6942–6951. [[CrossRef](#)]
6. Bai, W.; Ross, C.A. Functional nanostructured materials based on self-assembly of block copolymers. *MRS Bull.* **2016**, *41*, 100–107. [[CrossRef](#)]
7. Li, L.; Krissanasaeranee, M.; Pattinson, S.W.; Stefik, M.; Wiesner, U.; Steiner, U.; Eder, D. Enhanced photocatalytic properties in well-ordered mesoporous WO<sub>3</sub>. *Chem. Commun.* **2010**, *46*, 7620–7622. [[CrossRef](#)] [[PubMed](#)]
8. Hu, H.; Gopinadhan, M.; Osuji, C.O. Directed self-assembly of block copolymers: A tutorial review of strategies for enabling nanotechnology with soft matter. *Soft Matter* **2014**, *10*, 3867–3889. [[CrossRef](#)]
9. Dörr, T.S.; Fleischmann, S.; Zeiger, M.; Grobelsek, I.; de Oliveira, P.W.; Presser, V. Ordered Mesoporous Titania/Carbon Hybrid Monoliths for Lithium-ion Battery Anodes with High Areal and Volumetric Capacity. *Chem. Eur. J.* **2018**, *24*, 6358–6363. [[CrossRef](#)] [[PubMed](#)]
10. Dörr, T.S.; Pelz, A.; Zhang, P.; Kraus, T.; Winter, M.; Wiemhöfer, H.-D. An Ambient Temperature Electrolyte with Superior Lithium Ion Conductivity based on a Self-Assembled Block Copolymer. *Chem. Eur. J.* **2018**, *24*, 8061–8065. [[CrossRef](#)] [[PubMed](#)]
11. Pelz, A.; Dörr, T.S.; Zhang, P.; de Oliveira, P.W.; Winter, M.; Wiemhöfer, H.-D.; Kraus, T. Self-Assembled Block Copolymer Electrolytes: Enabling Superior Ambient Cationic Conductivity and Electrochemical Stability. *Chem. Mater.* **2019**, *31*, 277–285. [[CrossRef](#)]
12. Butzelaar, A.J.; Röring, P.; Mach, T.P.; Hoffmann, M.; Jeschull, F.; Wilhelm, M.; Winter, M.; Brunklus, G.; Théato, P. Styrene-Based Poly(ethylene oxide) Side-Chain Block Copolymers as Solid Polymer Electrolytes for High-Voltage Lithium-Metal Batteries. *ACS Appl. Mater. Interfaces* **2021**, *13*, 39257–39270. [[CrossRef](#)]
13. Flory, P.J. *Principles of Polymer Chemistry*, 16th ed.; Cornell University Press: Ithaca, NY, USA, 1995; pp. 541–593.
14. Bates, F.S. Polymer-Polymer Phase Behavior. *Science* **1991**, *251*, 898–905. [[CrossRef](#)]
15. Leibler, L. Theory of microphase separation in block copolymers. *Macromolecules* **1980**, *13*, 1602–1617. [[CrossRef](#)]
16. Lynd, N.A.; Meuler, A.J.; Hillmyer, M.A. Polydispersity and block copolymer self-assembly. *Prog. Polym. Sci.* **2008**, *33*, 875–893. [[CrossRef](#)]
17. Hillmyer, M.A.; Bates, F.S. Synthesis and Characterization of Model Polyalkane–Poly(ethylene oxide) Block Copolymers. *Macromolecules* **1996**, *29*, 6994–7002. [[CrossRef](#)]
18. Chatterjee, J.; Jain, S.; Bates, F.S. Comprehensive Phase Behavior of Poly(isoprene-*b*-styrene-*b*-ethylene oxide) Triblock Copolymers. *Macromolecules* **2007**, *40*, 2882–2896. [[CrossRef](#)]
19. Bailey, T.S.; Pham, H.D.; Bates, F.S. Morphological Behavior Bridging the Symmetric AB and ABC States in the Poly(styrene-*b*-isoprene-*b*-ethylene oxide) Triblock Copolymer System. *Macromolecules* **2001**, *34*, 6994–7008. [[CrossRef](#)]
20. Kimms, L.; Diddens, D.; Heuer, A. Understanding the Lithium Ion Transport in Concentrated Block–Copolymer Electrolytes on a Microscopic Level. *arXiv* **2020**, arXiv:2010.11673.
21. Kim, S.H.; Misner, M.J.; Xu, T.; Kimura, M.; Russell, T.P. Highly Oriented and Ordered Arrays from Block Copolymers via Solvent Evaporation. *Adv. Mater.* **2004**, *16*, 226–231. [[CrossRef](#)]
22. Sun, Y.; Tan, R.; Ma, Z.; Zhou, D.; Li, J.; Kong, D.; Dong, X.-H. Quantify the contribution of chain length heterogeneity on block copolymer self-assembly. *Giant* **2020**, *4*, 100037. [[CrossRef](#)]
23. Albert, J.N.; Epps, T.H. Self-assembly of block copolymer thin films. *Mater. Today* **2010**, *13*, 24–33. [[CrossRef](#)]
24. Epps, T.H.; Cochran, E.W.; Bailey, T.S.; Waletzko, R.S.; Hardy, C.M.; Bates, F.S. Ordered Network Phases in Linear Poly(isoprene-*b*-styrene-*b*-ethylene oxide) Triblock Copolymers. *Macromolecules* **2004**, *37*, 8325–8341. [[CrossRef](#)]
25. Coats, J.P.; Cochereau, R.; Dinu, I.A.; Messmer, D.; Sciortino, F.; Palivan, C.G. Trends in the Synthesis of Polymer Nano- and Microscale Materials for Bio-Related Applications. *Macromol. Biosci.* **2023**, 2200474. [[CrossRef](#)]
26. Xiang, L.; Li, Q.; Li, C.; Yang, Q.; Xu, F.; Mai, Y. Block Copolymer Self-Assembly Directed Synthesis of Porous Materials with Ordered Bicontinuous Structures and Their Potential Applications. *Adv. Mater.* **2023**, *35*, 2207684. [[CrossRef](#)]
27. Qi, H.; Xie, R.; Yang, G.-W.; Zhang, Y.-Y.; Xu, C.-K.; Wang, Y.; Wu, G.-P. Rational Optimization of Bifunctional Organoboron Catalysts for Versatile Polyethers via Ring-Opening Polymerization of Epoxides. *Macromolecules* **2022**, *55*, 9081–9090. [[CrossRef](#)]
28. Quirk, R.P.; Zhuo, Q.; Jang, S.H.; Lee, Y.; Lizarraga, G. *Applications of Anionic Polymerization Research*; Principles of Anionic Polymerization: An Introduction; American Chemical Society: Washington, DC, USA, 1998; pp. 2–27.

29. Jagur-Grodzinski, J. Functional polymers by living anionic polymerization. *J. Polym. Sci. Part A Polym. Chem.* **2002**, *40*, 2116–2133. [[CrossRef](#)]
30. Merck Ethylene Oxide. Available online: <https://www.sigmaaldrich.com/DE/en/product/sial/03906> (accessed on 28 March 2022).
31. Förster, S.; Krämer, E. Synthesis of PB–PEO and PI–PEO Block Copolymers with Alkylolithium Initiators and the Phosphazene Base *t*-BuP<sub>4</sub>. *Macromolecules* **1999**, *32*, 2783–2785. [[CrossRef](#)]
32. Herzberger, J.; Niederer, K.; Pohlit, H.; Seiwert, J.; Worm, M.; Wurm, F.R.; Frey, H. Polymerization of Ethylene Oxide, Propylene Oxide, and Other Alkylene Oxides: Synthesis, Novel Polymer Architectures, and Bioconjugation. *Chem. Rev.* **2016**, *116*, 2170–2243. [[CrossRef](#)] [[PubMed](#)]
33. Esswein, B.; Möller, M. Polymerization of Ethylene Oxide with Alkylolithium Compounds and the Phosphazene Base “*t*Bu-P<sub>4</sub>”. *Angew. Chem. Int. Ed. Engl.* **1996**, *35*, 623–625. [[CrossRef](#)]
34. Brocas, A.-L.; Mantzaridis, C.; Tunc, D.; Carlotti, S. Polyether synthesis: From activated or metal-free anionic ring-opening polymerization of epoxides to functionalization. *Prog. Polym. Sci.* **2013**, *38*, 845–873. [[CrossRef](#)]
35. Dreier, P.; Ahn, J.; Chang, T.; Frey, H. End Group Functionality of 95–99%: Epoxide Functionalization of Polystyryl-Lithium Evaluated via Solvent Gradient Interaction Chromatography. *Macromol. Rapid Commun.* **2022**, *43*, 2200560. [[CrossRef](#)] [[PubMed](#)]
36. Gao, T.; Xia, X.; Tajima, K.; Yamamoto, T.; Isono, T.; Satoh, T. Polyether/Polythioether Synthesis via Ring-Opening Polymerization of Epoxides and Episulfides Catalyzed by Alkali Metal Carboxylates. *Macromolecules* **2022**, *55*, 9373–9383. [[CrossRef](#)]
37. Quirk, R.P.; Pickel, D.L.; Hasegawa, H. Anionic Polymerization Chemistry of Epoxides: Electron-Transfer Processes. *Macromol. Symp.* **2005**, *226*, 69–78. [[CrossRef](#)]
38. Tonhauser, C.; Frey, H. A Road Less Traveled to Functional Polymers: Epoxide Termination in Living Carbanionic Polymer Synthesis. *Macromol. Rapid Commun.* **2010**, *31*, 1938–1947. [[CrossRef](#)]
39. Tonhauser, C.; Golriz, A.A.; Moers, C.; Klein, R.; Butt, H.-J.; Frey, H. Stimuli-Responsive Y-Shaped Polymer Brushes Based on Junction-Point-Reactive Block Copolymers. *Adv. Mater.* **2012**, *24*, 5559–5563. [[CrossRef](#)] [[PubMed](#)]
40. Natalello, A.; Alkan, A.; Friedel, A.; Lieberwirth, I.; Frey, H.; Wurm, F.R. Enlarging the Toolbox: Epoxide Termination of Polyferrocenylsilane (PFS) as a Key Step for the Synthesis of Amphiphilic PFS–Polyether Block Copolymers. *ACS Macro Lett.* **2013**, *2*, 313–316. [[CrossRef](#)] [[PubMed](#)]
41. Zhang, J.; Pointer, W.; Patias, G.; Al-Shok, L.; Hand, R.A.; Smith, T.; Haddleton, D.M. End functionalization of polyisoprene and polymyrcene obtained by anionic polymerization via one-pot ring-opening mono-addition of epoxides. *Eur. Polym. J.* **2023**, *183*, 111755. [[CrossRef](#)]
42. Pearson, R.G. Hard and soft acids and bases. *J. Am. Chem. Soc.* **1963**, *85*, 3533–3539.
43. Krause, D.; Grünebaum, M.; Wiemhöfer, H.-D.; Winter, M. Improved Synthesis for Producing Ordered Poly-Block Copolymers Having a Controllable Molecular Weight Distribution. International Patent Application No. PCT/WO 2022/008615 A1, 23 January 2023.
44. Lochmann, L.; Pospíšil, J.; Lim, D. On the interaction of organolithium compounds with sodium and potassium alkoxides. A new method for the synthesis of organosodium and organopotassium compounds. *Tetrahedron Lett.* **1966**, *7*, 257–262. [[CrossRef](#)]
45. Long, T.E.; Liu, H.Y.; Schell, B.A.; Teegarden, D.M.; Uerz, D.S. Determination of solution polymerization kinetics by near-infrared spectroscopy. 1. Living anionic polymerization processes. *Macromolecules* **1993**, *26*, 6237–6242. [[CrossRef](#)]
46. Fulmer, G.R.; Miller, A.J.M.; Sherden, N.H.; Gottlieb, H.E.; Nudelman, A.; Stoltz, B.M.; Bercaw, J.E.; Goldberg, K.I. NMR Chemical Shifts of Trace Impurities: Common Laboratory Solvents, Organics, and Gases in Deuterated Solvents Relevant to the Organometallic Chemist. *Organometallics* **2010**, *29*, 2176–2179. [[CrossRef](#)]
47. Biehl, R. Jscatter, a program for evaluation and analysis of experimental data. *PLoS ONE* **2019**, *14*, e0218789. [[CrossRef](#)] [[PubMed](#)]
48. Förster, S.; Apostol, L.; Bras, W. Scatter: Software for the analysis of nano- and mesoscale small-angle scattering. *J. Appl. Crystallogr.* **2010**, *43*, 639–646. [[CrossRef](#)]
49. Graf, M. Polarmodifikation von Butadienkautschuk mit Polyethylenglykol. Ph.D. Thesis, Universität Bayreuth, Bayreuth, Germany, 28 October 2002.
50. Zhang, B.; Zhang, Y.; Zhang, N.; Liu, J.; Cong, L.; Liu, J.; Sun, L.; Mauger, A.; Julien, C.M.; Xie, H.; et al. Synthesis and interface stability of polystyrene-poly(ethylene glycol)-polystyrene triblock copolymer as solid-state electrolyte for lithium-metal batteries. *J. Power Sources* **2019**, *428*, 93–104. [[CrossRef](#)]
51. Liu, Y.; Wang, Y.; Wang, Y.; Lu, J.; Piñón, V.; Weck, M. Shell Cross-Linked Micelle-Based Nanoreactors for the Substrate-Selective Hydrolytic Kinetic Resolution of Epoxides. *J. Am. Chem. Soc.* **2011**, *133*, 14260–14263. [[CrossRef](#)] [[PubMed](#)]
52. van Butsele, K.; Stoffelbach, F.; Jérôme, R.; Jérôme, C. Synthesis of Novel Amphiphilic and pH-Sensitive ABC Miktoarm Star Terpolymers. *Macromolecules* **2006**, *39*, 5652–5656. [[CrossRef](#)]
53. Bhanu, V.A.; Kishore, K. Role of oxygen in polymerization reactions. *Chem. Rev.* **1991**, *91*, 99–117. [[CrossRef](#)]
54. Wurm, F.; Wilms, D.; Klos, J.; Löwe, H.; Frey, H. Carbanions on Tap–Living Anionic Polymerization in a Microstructured Reactor. *Macromol. Chem. Phys.* **2008**, *209*, 1106–1114. [[CrossRef](#)]
55. Castle, T.C. Synthesis of Block Copolymers by the Conversion of Living Anionic Polymerisation Into Living ROMP. Ph.D. Thesis, Durham University, Durham, UK, 13 June 2005.
56. Chang, N.N.; Daly, S.R.; Girolami, G.S. Salt elimination reactions do not always eliminate. Mechanistic study of the reaction of NdCl<sub>3</sub> with sodium *N,N*-dimethylaminodiborane. *Polyhedron* **2019**, *162*, 52–58. [[CrossRef](#)]
57. Surakit, T.; Adun, N.; Jitladda, T.S. Quantitative analysis of isoprene units in natural rubber and synthetic polyisoprene using <sup>1</sup>H-NMR spectroscopy with an internal standard. *Polym. Test.* **2015**, *43*, 21–26.

58. Toolan, D.T.W.; Isakova, A.; Hodgkinson, R.; Reeves-McLaren, N.; Hammond, O.S.; Edler, K.J.; Briscoe, W.H.; Arnold, T.; Gough, T.; Topham, P.D.; et al. Insights into the Influence of Solvent Polarity on the Crystallization of Poly(ethylene oxide) Spin-Coated Thin Films via In Situ Grazing Incidence Wide-Angle X-ray Scattering. *Macromolecules* **2016**, *49*, 4579–4586. [[CrossRef](#)]
59. Butzelaar, A.J.; Röring, P.; Hoffmann, M.; Atik, J.; Paillard, E.; Wilhelm, M.; Winter, M.; Brunklaus, G.; Theato, P. Advanced Block Copolymer Design for Polymer Electrolytes: Prospects of Microphase Separation. *Macromolecules* **2021**, *54*, 11101–11112. [[CrossRef](#)]
60. Sakurai, S.; Momii, T.; Taie, K.; Shibayama, M.; Nomura, S.; Hashimoto, T. Morphology transition from cylindrical to lamellar microdomains of block copolymers. *Macromolecules* **1993**, *26*, 485–491. [[CrossRef](#)]
61. Fetters, L.J.; Lohse, D.J.; Richter, D.; Witten, T.A.; Zirkel, A. Connection between Polymer Molecular Weight, Density, Chain Dimensions, and Melt Viscoelastic Properties. *Macromolecules* **1994**, *27*, 4639–4647. [[CrossRef](#)]
62. Isono, T.; Kawakami, N.; Watanabe, K.; Yoshida, K.; Otsuka, I.; Mamiya, H.; Ito, H.; Yamamoto, T.; Tajima, K.; Borsali, R. Microphase separation of carbohydrate-based star-block copolymers with sub-10 nm periodicity. *Polym. Chem.* **2019**, *10*, 1119–1129. [[CrossRef](#)]
63. Chintapalli, M.; Le, T.N.P.; Venkatesan, N.R.; Mackay, N.G.; Rojas, A.A.; Thelen, J.L.; Chen, X.C.; Devaux, D.; Balsara, N.P. Structure and Ionic Conductivity of Polystyrene-*block*-poly(ethylene oxide) Electrolytes in the High Salt Concentration Limit. *Macromolecules* **2016**, *49*, 1770–1780. [[CrossRef](#)]
64. Zhu, L.; Cheng, S.Z.D.; Calhoun, B.H.; Ge, Q.; Quirk, R.P.; Thomas, E.L.; Hsiao, B.S.; Yeh, F.; Lotz, B. Phase structures and morphologies determined by self-organization, vitrification, and crystallization: Confined crystallization in an ordered lamellar phase of PEO-*b*-PS diblock copolymer. *Polymer* **2001**, *42*, 5829–5839. [[CrossRef](#)]
65. Michler, G.H. *Electron Microscopy of Polymers*; Preparation of Thin Sections: (Cryo)ultramicrotomy and (Cryo)microtomy; Springer Laboratory: Berlin/Heidelberg, Germany, 2008; pp. 199–217.

**Disclaimer/Publisher’s Note:** The statements, opinions and data contained in all publications are solely those of the individual author(s) and contributor(s) and not of MDPI and/or the editor(s). MDPI and/or the editor(s) disclaim responsibility for any injury to people or property resulting from any ideas, methods, instructions or products referred to in the content.